


 Cite this: *RSC Adv.*, 2025, 15, 18089

Synthesis and multifaceted exploration of dibenzoxepinones: *in vitro* antimicrobial and ct-DNA binding, DFT/TD-DFT, molecular docking and simulation studies†

 Shilpa Yadav,^a Mansi,^{id}^a Priyanshu,^b Pratibha Chanana,^b Pankaj Khanna,^{id}^c Asmita Singh^a and Leena Khanna^{id}^{*a}

In the present study, ten novel derivatives of dibenzoxepine-11-one, have been synthesized and thoroughly characterized using spectroscopic techniques, including ¹H and ¹³C NMR, FTIR, and HRMS. Density Functional Theory (DFT) calculations were carried out to analyze the geometrical structure and vibrational modes, enabling the identification of the most stable conformation of the lead compound. Time-Dependent DFT (TD-DFT) was employed to investigate the electronic transitions within the UV-Vis spectrum. Molecular docking studies were performed for all derivatives using various target proteins with PDB IDs: IKZN (for *E. coli*), 1IYL (for *C. albicans*), and the DNA dodecamer structure (PDB ID: 1BNA). The results revealed favorable binding interactions across all targets. Additionally, molecular dynamics (MD) simulations were conducted for 50 ns using the most promising compound, **7a**, confirming the stability of its binding conformation. From *in vitro* studies, antibacterial activity was assessed for all the synthesized derivatives against Gram-positive strains (*B. subtilis*, *L. rhamnosus*) and a Gram-negative strain (*E. coli*). Compounds **7a**, **7b**, **7c**, **7d**, and **7f** exhibited strong antibacterial efficacy, with minimum inhibitory concentration (MIC) values of 8 μg ml⁻¹ for *E. coli* and *L. rhamnosus* and 16 μg ml⁻¹ for *B. subtilis* bacterial strains. Additionally, compound **7a** exhibited good antifungal activity, with a maximum zone of inhibition of 18 mm against the fungal strain *C. albicans*. Further UV-Vis absorption and fluorescence quenching studies, conducted for compounds **7a**, **7b**, and **7e** with calf thymus DNA (ct-DNA), suggested a groove-binding interaction. Compound **7a** demonstrated the strongest binding affinity, with a binding constant (*K*_b) of 3.61 × 10⁵ M⁻¹ and a Gibbs free energy change (Δ*G*) of -31.70 kJ mol⁻¹. Therefore, these novel dibenzoxepine-11-ones derivatives are multifaceted in their action as potential antimicrobial and DNA-binding agents, and will be useful in developing new therapeutics.

 Received 13th February 2025
 Accepted 15th May 2025

DOI: 10.1039/d5ra01068c

rsc.li/rsc-advances

1. Introduction

Dibenzoxepinone is a tricyclic heterocycle featuring two fused benzene rings and a seven-membered oxepine ring. This chemical structure serves as the foundation for various pharmacological applications such as antibacterial, antifungal, antitumor, antihistamine, antidepressant, and anti-inflammatory.¹⁻³ A

prominent example of a dibenzoxepinone derivative is doxepin, which treats depression, anxiety, and chronic skin conditions such as urticaria.^{4,5} Its other derivatives, such as Oxepinoquinones and Naphthodibenzoxepine, disrupt bacterial membrane integrity, leading to bacterial cell death and also preventing bacterial DNA replication. Halogenated dibenzoxepinone inhibits fungal membrane integrity and reduces infection persistence.⁶ These compounds often disrupt bacterial cell walls, inhibit DNA replication, or target specific bacterial enzymes. Modifying the core dibenzoxepinone framework can improve antibacterial activity against various bacterial strains, including both Gram-negative and Gram-positive bacteria.⁷ Furthermore, additional derivatives of dibenzoxepinone are under investigation as potential anticancer agents, as their structure can be altered to interact with key processes in cancer cells. They have the potential to block cancer cell growth by interfering with DNA, inhibiting crucial enzymes, or triggering cell death.^{8,9} Thus, motivated by the

^aUniversity School of Basic & Applied Sciences, Guru Gobind Singh Indraprastha University, Dwarka, New Delhi-110078, India. E-mail: leenakhanna@ipu.ac.in

^bUniversity School of Chemical Technology, Guru Gobind Singh Indraprastha University, Dwarka, New Delhi-110078, India

^cSynthesis & In-Silico Drug Design Laboratory, Department of Chemistry, Acharya Narendra Dev College, University of Delhi, Kalkaji, New Delhi-110019, India

† Electronic supplementary information (ESI) available: Spectroscopy spectrums, molecular docking binding energy tables, ADME, and physicochemical properties and DFT calculations of all the derivatives can be accessed here. See DOI: <https://doi.org/10.1039/d5ra01068c>



diverse importance of dibenzoxepinone and as active researchers of heterocyclic compounds,^{10–14} we propose synthesizing novel derivatives of dibenzoxepin-11-one. The methodology involves synthesizing dibenzoxepin-11-one, followed by introducing various amines to one of its aromatic rings *via* a plausible route to assess their biological applications. Ten novel compounds were prepared and characterized using various spectroscopic techniques. DFT studies provided a potential energy scan for different conformations of the best compound. UV and FTIR calculations were also performed to observe the electronic transitions and vibrations of the compound and compare the data with the experimental results.^{15,16} Molecular docking was conducted with potential targets of antibacterial, antifungal, and ct-DNA using PDB IDs: 1KZN, 1IYL, and 1BNA through AutoDock 4.2.^{17–19} This aimed to determine the binding energy and uncover how proteins interact with ligands, along with the types of bonds formed between proteins and ligands. An MD simulation study was carried out for 50 ns to evaluate the stability of the protein-ligand complex in a biological system.^{20,21} Antibacterial and antifungal *in vitro* studies were performed to inhibit the growth of bacterial strains (*E. coli*, *L. rhamnosus* and *B. subtilis*) and a fungal strain (*C. albicans*) by MIC and Zone of inhibition. Additionally, UV-vis absorption and fluorescence quenching *in vitro* experiments were conducted to evaluate the DNA binding abilities of the dibenzoxepinone derivatives.^{22,23}

2. Experimental techniques

2.1 Materials and methods

Reagents used in the synthesis of products were purchased from Sigma Aldrich. Positive control drugs Ampicillin and Fluconazole were purchased from SRL. Solvents were purchased by Merck and SRL. TLC plates of silica gel mesh 60F₂₅₄ (Merck) were used as a preliminary test to check the progress of the reaction by the spots located in UV and Iodine vapors. Jeol Spectrometer of 400 MHz was used for ¹H and ¹³C (TMS as a reference). FTIR spectra were recorded by PerkinElmer Spectrum BX spectrophotometer. HRMS was recorded by ESI-MS Thermo LTQ Orbitrap XL in methanol. Absorbance for the ct-DNA binding activity and UV Fluorescence quenching study property was taken by UV-1900 Shimadzu UV VIS Spectrophotometer, Double Beam.

2.2 Synthesis

Dibenzoxepinone derivatives were synthesized in four steps. First step involved the formation of aryl benzyl ether (3) *via* Williamson ether synthesis. The second step is the cyclodehydration or intramolecular Friedel-Crafts acylation reaction using lewis acid FeCl₃ and DCME to form dibenzoxepin-11-one (4). Third step is bromination of methyl group present in the aromatic ring of dibenzoxepin-11-one *via* Wohl-Ziegler bromination reaction *i.e.* allylic bromination using with *N*-bromosuccinimide. Fourth step is the nucleophilic displacement of bromine group by various aliphatic and aromatic amines to get the desired novel dibenzoxepinone derivatives (7a–j) as the product.^{24–27}

2.2.1 Synthesis for 2-((*o*-tolyl oxy)methyl)benzoic acid (3). 1 mmol of *o*-cresol (2) and 1.5 mmol of KH was added to the

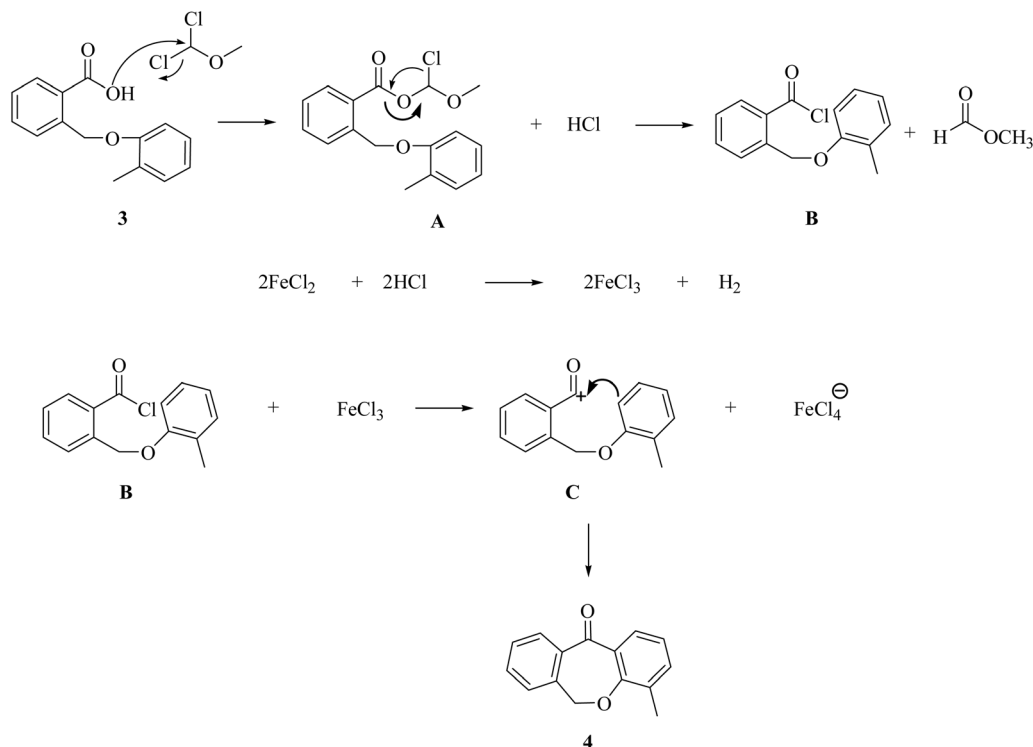
15 ml of dry DMF under nitrogen, stirred the reaction mixture for 15–20 min. Then, 1 mmol of phthalide (1) solution in toluene was added, and the reaction mixture was refluxed for 24 h. Ice-cooled water was added to quench the reaction and then acidified with conc. HCl and residue obtained was filtered.²⁸ Color-pale yellow, yield 75%, mp 116–118 °C; ¹H-NMR (400 MHz, CDCl₃): δ 2.34 (s, 1H, CH₃), 5.52 (s, 2H, O-CH₂), 6.87 (m, 2H, ArH), 7.14 (m, 2H, Ar-H), 7.40 (t, 1H, *J* = 8Hz, ArH) 7.62 (t, 1H, *J* = 8Hz, ArH), 7.84 (t, 1H, *J* = 8Hz), 8.13 (d, 1H, *J* = 8Hz). HRMS calcd [M + H]⁺ for C₁₅H₁₄O₃: 243.0979, found: 243.1024.

2.2.2 Synthesis for 4-methyl-6H-dibenzo[*b,e*]oxepine-11-one (4). 1 mmol of synthesized product (3), 1.5 mmol of anhydrous FeCl₂ or anhydrous CeCl₃, 1 mmol of DCME (dichloromethyl methyl ether) were added in DCM under nitrogen and stirred for 4 h at room temperature. It was mentioned in the literature that by using different Lewis acid catalysts like SnCl₄, FeCl₃, AlCl₃, and FeBr₃ for this intramolecular cyclization, no or less yield was obtained but the maximum yield was found in the case of FeCl₂.²⁸ However, when we have taken a new Lewis acid catalyst CeCl₃,²⁹ and observed that FeCl₂ formed the product in 90% yield while CeCl₃ formed the product in 65% only. Color – light yellow, yield 70%, mp 132–133 °C; ¹H-NMR (400 MHz, CDCl₃): δ 2.26 (s, 1H, CH₃), 5.22 (s, 2H, O-CH₂), 7.00 (t, 1H, *J* = 8Hz, ArH), 7.36 (t, 1H, *J* = 8Hz, Ar-H), 7.45 (m, 2H, ArH). 7.54 (t, 1H, *J* = 8Hz, ArH), 7.86 (d, 1H, *J* = 8Hz), 8.06 (d, 1H, *J* = 8Hz). ¹³C-NMR: δ 16.81 (CH₃), 73.62 (O-CH₂), 121.58, 127.62, 129.29, 129.42, 129.52, 129.86, 132.66, 135.85, 136.44 (aromatic region). HRMS calcd [M + H]⁺ for C₁₅H₁₂O₂: 225.0869, found: 225.1024 (Scheme 1).

For this step we have proposed a mechanism to highlight the importance of Lewis acid FeCl₂ over FeCl₃ in this cyclization. This is an intramolecular cyclization *via* the Friedel-Crafts acylation mechanism in which a molecule containing both an aromatic ring and an acyl group forms cyclic ketone. The reaction begins with the conversion of the carboxylic group into an acid chloride group in the presence of DCME (dimethyl methyl ether) which is a well-known reagent for this conversion to form intermediate acid chloride (B) *via* A.³⁰ In this process HCl is liberated which reacts with FeCl₂ to generate FeCl₃ *in situ*. The FeCl₃ further acts as a lewis acid for B and helps to generate acylium ion (C).³¹ The acylium group then attacks the aromatic ring and intramolecular acylation occurs within the same molecule and creating a new cyclic structure as 4-methyl-dibenzoxepin-11-one (4).

2.2.3 Synthesis for 4-bromomethyl-6H-dibenzo[*b,e*]oxepine-11-one (5). 1 mmol of (4), 1.5 mmol of NBS (*N*-bromosuccinimide), 2 mmol of DBP (dibenzoyl peroxide) were mixed in CCl₄, after 10–15 min. The red-colored solution was observed, then again stirred the reaction mixture until the red color disappeared. The solution was kept stirred for 2 h and then added water, extracted by ethyl acetate, and evaporated the organic layer to get the product.³² Color – yellow, yield 95%, mp 103–105 °C; ¹H-NMR (400 MHz, CDCl₃): δ 3.49 (s, 2H, CH₂-Br) 5.20 (s, 2H, O-CH₂), 7.07 (m, ArH), 7.44 (m, Ar-H). ¹³C-NMR: δ 29.81 (CH₂ Br), 74.20 (O-CH₂), 120.83, 122.35, 128.10, 129.60, 129.78, 132.26, 133.03, 135.60, 135.66, 161.42 (carbonyl carbon). HRMS calcd [M + H]⁺ for C₁₅H₁₁BrO₂: 301.99, found: 303.0006.





Scheme 1 Plausible mechanism of intramolecular cyclization for step (ii).

2.2.4 Synthesis of (7a–j). 1 mmol of different amines (**6a–j**), 1.5 mmol of KH was taken in 15 ml dry DMF under nitrogen after stirring of 15–20 min, 1 mmol of **5** was added to it and again stirred for 22 h at ambient temperature. The reaction was quenched with ice-cooled water and the product was extracted from ethyl acetate and the solvent was evaporated to get the desired product.²⁷ All these compounds were fully characterized by various spectroscopic techniques and the spectrums were provided in a ESI file.†

2.2.5 7-(*p*-Tolylamino-methyl)-6*H*-dibenzo[*b,e*]oxepin-11-one (7a). Color – brown, yield 94%, mp 324–327 °C; ¹H-NMR (400 MHz, CDCl₃): δ 2.13 (s, 3H, CH₃), 4.45 (s, 1H, NH), 4.95 (s, 2H, N-CH₂), 5.25 (s, 2H, O-CH₂), 6.93 (t, 2H, *J* = 8Hz, ArH), 7.10 (m, 3H, Ar-H), 7.41 (d, 2H, *J* = 8Hz, Ar-H), 7.53 (d, 2H, *J* = 8Hz, Ar-H), 7.70 (m, 3H-Ar-H). ¹³C-NMR: δ 16.84 (CH₃), 50.80 (N-CH₂), 73.62 (O-CH₂), 121.58, 127.62, 129.29, 129.42, 129.52, 129.86, 132.66, 136.44, 142.68, 145.87, 146.45 (aromatic region). HRMS calcd [M + H]⁺ for C₂₂H₁₉NO₂: 330.14, found: 330.1520.

2.2.6 7-[(*p*-Chloro-phenylamino)-methyl]-6*H*-dibenzo[*b,e*]oxepin-11-one (7b). Color – light brown, yield 97%, mp 356–358 °C; ¹H-NMR (400 MHz, CDCl₃): δ 4.12 (s, 1H, NH), 4.98 (s, 2H, N-CH₂), 5.24 (s, 2H, O-CH₂), 6.87 (t, 2H, *J* = 8Hz, ArH), 7.18 (m, 3H, Ar-H), 7.40 (t, 2H, *J* = 8Hz, ArH), 7.62 (d, 2H, *J* = 8Hz, ArH), 7.84 (d, 1H, *J* = 8Hz, Ar-H), 8.14 (m, 1H, Ar-H). ¹³C-NMR: δ 55.41 (N-CH₂), 74.06 (O-CH₂), 114.44, 114.68, 114.93, 117.35, 124.03, 127.29, 128.27, 128.68, 129.93, 130.07, 130.29, 133.16, 138.06, 153.45, 170.80 (carbonyl carbon). HRMS calcd [M + H]⁺ for C₂₁H₁₆ClNO₂: 351.09, found: 351.0979.

2.2.7 7-[(*p*-Fluoro-phenylamino)-methyl]-6*H*-dibenzo[*b,e*]oxepin-11-one (7c). Color – light brown, yield 95%, mp 275–

276 °C; ¹H-NMR (400 MHz, CDCl₃): δ 4.01 (s, 1H, NH), 4.76 (s, 2H, N-CH₂), 4.95 (s, 2H, N-CH₂), 5.21 (s, 2H, O-CH₂), 6.87 (t, 2H, *J* = 8Hz, Ar-H), 7.18 (m, 2H, ArH), 7.40 (t, 2H, *J* = 8Hz, Ar-H), 7.62 (t, 2H, *J* = 8Hz, Ar-H), 7.84 (d, 2H, Ar-H), 8.14 (d, 1H, *J* = 8Hz, Ar-H). ¹³C-NMR: δ 52.80 (N-CH₂), 54.99 (N-CH₂), 72.94 (O-CH₂), 119.99, 121.86, 122.87, 124.01, 126.55, 129.88, 131.00, 132.86, 133.87, 142.99, 147.45, 170.45 (carbonyl carbon). HRMS calcd [M + H]⁺ for C₂₂H₁₈FNO₂: 348.13, found: 348.1407.

2.2.8 7-[(Benzylamino-methyl)-6*H*-dibenzo[*b,e*]oxepin-11-one (7d). Color – brown, yield 97%, mp 249–250 °C; ¹H-NMR (400 MHz, CDCl₃): δ 4.46 (s, 1H, NH), 4.81 (s, 2H, N-CH₂), 5.06 (s, 2H, N-CH₂), 5.18 (s, 2H, O-CH₂), 6.92 (t, 1H, *J* = 8Hz, Ar-H), 7.09 (m, 2H, ArH), 7.13 (m, 3H, ArH), 7.82 (d, 2H, *J* = 8Hz, Ar-H), 8.22 (d, 1H, *J* = 8Hz, Ar-H), 8.34 (d, 2H, *J* = 8Hz, Ar-H). ¹³C-NMR: δ 46.85 (N-CH₂), 52.49 (N-CH₂), 75.47 (O-CH₂), 128.46, 128.85, 129.29, 129.78, 130.17, 133.74, 137.28, 137.77, 138.16, 141.74, 142.28, 171.81 (carbonyl carbon). HRMS calcd [M + H]⁺ for C₂₂H₁₉NO₂: 330.09, found: 330.1494.

2.2.9 7-[(*p*-Bromo-phenylamino)-methyl]-6*H*-dibenzo[*b,e*]oxepin-11-one (7e). Color – brown, yield 95%, mp 360–363 °C; ¹H-NMR (400 MHz, CDCl₃): δ 4.73 (s, 1H, NH), 4.99 (s, 2H, N-CH₂), 5.34 (s, 2H, O-CH₂), 6.89 (m, 2H, ArH), 7.39 (t, 1H, *J* = 8Hz, Ar-H), 7.61 (t, 1H, *J* = 8Hz, Ar-H), 7.85 (d, 2H, *J* = 8Hz, Ar-H), 7.93 (d, 1H, *J* = 8Hz, Ar-H), 8.15 (d, 2H, *J* = 8Hz, Ar-H), 8.23 (m, 2H, Ar-H). ¹³C-NMR: δ 52.64 (N-CH₂), 73.62 (O-CH₂), 121.58, 127.62, 129.29, 129.42, 129.52, 129.86, 132.66, 135.85, 136.44, 141.57, 147.62, 149.29, 149.42, 149.52, 149.85, 152.66, 155.85, 156.44 (aromatic region). HRMS calcd [M + H]⁺ for C₂₁H₁₆BrNO₂: 394.04, found: 394.0433.



2.2.10 7-[(*p*-Nitro-phenylamino-methyl)]-6*H*-dibenzo[*b,e*]oxepin-11-one (7f). Color – yellow, yield 96%, mp 355–356 °C; ¹H-NMR (400 MHz, CDCl₃): δ 4.45 (s, 1H, NH), 4.83 (s, 2H, N-CH₂), 5.14 (s, 2H, O-CH₂), 6.94 (t, 2H, *J* = 8Hz, Ar-H), 7.15 (m, 3H, ArH), 7.39 (t, 1H, *J* = 8Hz, Ar-H), 7.51 (t, 1H, *J* = 8Hz, Ar-H), 7.63 (m, 3H, Ar-H), 7.94 (d, 1H, *J* = 8Hz, Ar-H). ¹³C-NMR: δ 50.84 (N-CH₂), 73.62 (O-CH₂), 127.62, 129.29, 129.42, 129.52, 129.86, 132.66, 135.85, 136.44, 142.68, 145.87, 146.45, 151.50 (aromatic region). HRMS calcd [M + H]⁺ for C₂₁H₁₆N₂O₄: 361.11, found: 361.1921.

2.2.11 7-[(*tert*-Butylamino-methyl)]-6*H*-dibenzo[*b,e*]oxepin-11-one (7g). Color – light brown, yield 87%, mp 233–236 °C; ¹H-NMR (400 MHz, CDCl₃): δ 1.35 (s, 9H, 3CH₃), 3.92 (s, 1H, NH), 4.54 (s, 2H, N-CH₂), 5.24 (s, 2H, O-CH₂), 6.98 (m, 2H, Ar-H), 7.28 (t, 1H, *J* = 8Hz, ArH), 7.39 (t, 1H, *J* = 8Hz, Ar-H), 7.60 (t, 1H, *J* = 8Hz, Ar-H), 7.78 (d, 1H, *J* = 8Hz, Ar-H), 8.13 (d, 1H, *J* = 8Hz, Ar-H). ¹³C-NMR: δ 14.14 (*tert*-C), 22.71 (C-CH₃), 29.17 (C-CH₃), 31.63 (C-CH₃), 76.71 (O-CH₂), 114.08, 115.90, 123.49, 124.03, 135.16, 139.29, 142.80, 151.91 (aromatic region). HRMS calcd [M + H]⁺ for C₁₉H₂₁NO₂: 296.16, found: 296.1453.

2.2.12 7-(Allylamino-methyl)-6*H*-dibenzo[*b,e*]oxepin-11-one (7h). Colour – light brown, yield 85%, mp 213–216 °C; ¹H-NMR (400 MHz, CDCl₃): δ 3.92 (t, 2H, *J* = 8Hz, C-CH₂), 4.52 (d, 2H, *J* = 8Hz, N-CH₂), 5.02 (s, 2H, N-CH₂), 5.52 (s, 2H, O-CH₂), 5.62 (d, 2H, allyl protons), 6.98 (t, 2H, *J* = 8Hz, Ar-H), 7.28 (m, 3H, ArH), 7.41 (t, 1H, *J* = 8Hz, Ar-H), 7.58 (t, 1H, *J* = 8Hz, Ar-H), 7.78 (m, 1H, Ar-H), 8.12 (m, 1H, Ar-H). ¹³C-NMR: δ 33.74 (N-CH₂), 34.84 (N-CH₂), 76.70, 114.07, 115.89, 123.48, 124.01, 128.61, 135.15, 139.27, 142.73, 151.97 (aromatic region). HRMS calcd [M + H]⁺ for C₁₈H₁₇NO₂: 280.13, found: 280.1407.

2.2.13 7-[(*p*-Methoxy-phenylamino-methyl)]-6*H*-dibenzo[*b,e*]oxepin-11-one (7i). Color – dark brown, yield 94%, mp 373–375 °C; ¹H-NMR (400 MHz, CDCl₃): δ 3.52 (s, 3H, OCH₃), 4.45 (s, 1H, NH), 4.95 (s, 2H, N-CH₂), 5.25 (s, 2H, O-CH₂), 6.94 (t, 2H, *J* = 8Hz, Ar-H), 7.10 (m, 2H, ArH), 7.39 (d, 2H, *J* = 8Hz, Ar-H), 7.54 (d, 2H, *J* = 8Hz, Ar-H), 7.73 (m, 3H, Ar-H). ¹³C-NMR: δ 35.00 (O-CH₃), 54.46 (N-CH₂), 74.25 (O-CH₂), 118.02, 119.54, 126.92, 128.74, 130.78, 132.40, 132.23, 138.01, 139.53, 142.55, 144.01, 145.53 (aromatic region). HRMS calcd [M + H]⁺ for C₂₂H₁₉NO₃: 346.14, found: 346.1453.

2.2.14 7-(Octadecyl methyl)-6*H*-dibenzo[*b,e*]oxepin-11-one (7j). Color – dark brown, yield 88%, mp 210–211 °C; ¹H-NMR (400 MHz, CDCl₃): δ 0.98 (m, 4H), 1.13–1.25 (m, 26H), 4.31 (s, N-H, 1H), 4.50 (s, 2H, oleyl chain N-CH₂), 5.22 (s, 2H, O-CH₂), 5.32 (m, 2H, -CH=CH-, oleyl chain), 7.12 (m, 3H, ArH), 7.53 (t, 2H, *J* = 8Hz, Ar-H), 7.82 (d, 1H, Ar-H, *J* = 8Hz), 8.11 (d, 2H, Ar-H, *J* = 8Hz). ¹³C-NMR: δ 11.42, 14.42, 19.73, 22.70, 26.85, 27.18, 29.38, 30.05, 32.76, 38.22 (aliphatic region), 121.3, 129.74, 129.98, 132.82, 161.20, 164.78 (carbonyl carbon). HRMS calcd [M + H]⁺ for C₃₃H₄₉NO₂: 492.38, found: 492.3755.

3. *In silico* study

3.1 DFT study

A Density Functional Theory study is a computational quantum model used to investigate the electronic structure, energy levels, molecular orbitals, and mechanism of

a compound. DFT study also helps to find out the theoretical NMR, FTIR, and UV-visible. The desired structure is first made in Gauss view 6.0 and set the calculation for optimization in Gaussian 09W at B3LYP/6-31+G(d,p) basis set. After optimizing the structure, the Potential energy surface (PES) study was performed on the flexible bonds by changing the bond angle from 90° to 120° by a transformation of 0.5° and the bond length of the NH bond by 0.05 Å each time of compound 7a.¹⁵ The frequency calculation was also done on the same basis set for analyzing the vibrations in a compound as FTIR spectra.^{33,34} No imaginary frequency in the output file approves the stationary state of the compound. Further, a UV-visible theoretical study was performed *via* the TD-SCF method at B3LYP/6-31+G(d,p) basis set.³⁵ UV-visible and FTIR theoretical results were compared with experimental data.

3.2 Molecular docking

3.2.1 Protein preparation. The crystal structure of different proteins DNA gyrase (PDB ID:1KZN, antibacterial), *N*-myristoyl-transferase (PDB ID:1IYL, antifungal), and DNA dodecamer (PDB ID:1BNA, ct-DNA activity) as drug targets were chosen from RCSB Protein Data Bank (<https://www.pdb.org>) were attained from RCSB Protein Data Bank.^{36–38} All crystal structures have more than 1 subunit of proteins, so all the chains except chain A, water molecules, and hetero atoms were removed. During the process, Kollman charges and polar hydrogen atoms were added to chain A which also includes some different amino acids for binding with ligands.

3.2.2 Binding site. The binding site refers to the specific region of a target molecule, usually a protein, where a ligand binds. It is typically composed of a specific amino acid residue on the protein surface or within a cavity that interacts with the ligands through various forces. Table 2 mentions the binding sites of different proteins, such as clorobiocin, *N*-myristoyl-transferase, and DNA dodecamer.

3.2.3 Validation of docking. The crystal structures of DNA gyrase and *N*-myristoyl transferase proteins are bound to chain A. The active sites were identified by consulting binding site information from the literature and visualizing it using Biovia Discovery Studio 2021.³⁹ The docking procedure was validated by redocking the extracted DNA gyrase and *N*-myristoyl transferase substrate with chain A of the IKZN and 1IYL protein using the same coordinates. Docking accuracy was evaluated based on the RMSD score, which ideally should be less than 2 Å. This validation step is crucial for assessing the reliability of the chosen docking methodology.

3.2.4 Docking procedure. The compounds were subjected to molecular docking using AutoDock 4.2. All the compounds and proteins were set in a cubic grid box having dimensions 60 Å (12.614x, 47.765y, -0.440z) for antifungal activity against *C. albicans* (PDB:1D:1IYL), 60 Å (19.577x, 19.108y, 43.257z) for antibacterial activity against *E. coli* (PDB:ID 1KZN), and 120 Å (15.091x, 21.550y, 8.822z) for ct-DNA (PDB:ID 1BNA) with a default spacing 0.375 Å. 10 conformations were obtained for every compound and a grid map was added using Autogrid 4.2. Docking calculation was performed by using AutoDock 4.2. The



analysis of interactions between the protein and compounds was evaluated using Biovia Discovery Studio 2021.

3.3 ADME and physicochemical (drug likeliness) properties

ADME study analyses the chemical behavior of pharmacological compounds in a living organism. All the pharmacokinetic parameters were calculated from the PreADMET online server. This study helps to find out the detailed behavior of compounds by absorption, distribution, metabolism, and excretion in the body. These factors are crucial in drug development and its therapeutic effects and minimizing the side effects. Numerous parameters such as Blood–brain Barrier (BBB), Plasma Protein Binding (PPB), Skin permeability, *etc.*, are used to describe drug toxicity.⁴⁰

Physicochemical parameters help to predict whether a compound has some features to become an effective drug or not. The parameters such as $\log P$, PSA (Polar Surface Area), molecular weight, no. of heavy atoms, *etc.*, were calculated from <https://www.molinspiration.com>. All these parameters are a set of guidelines for Lipinski's rule that assess the drug likeliness of a compound. Any compound with only one violation of Lipinski's rule becomes an orally active drug.⁴¹

Bioactivity scores, such as those of GPCR ligands, kinase or protease inhibitors, and ion exchange modulators, illustrate the relationship between drugs and receptors. The mol-inspiration online server (<https://www.molinspiration.com>) helps to calculate the bioactivity score of ligands. Any drug is considered to be active if its bioactivity score is greater than 0.0, moderately active if its score lies between -5.0 and 0.0 , and inactive if the score is lesser than -5.0 .⁴²

3.4 MD simulation

The optimal ligand **7a** was subjected to molecular dynamics (MD) simulations by GROMACS (Version 2020) to assess the stability of docked complexes.⁴³ The PRODRG server-generated ligand topology files, and GROMOS96_43a1 applied the force field for the simulations, which were conducted over 50 nanoseconds. The protein–ligand combination was solubilized in a cubic box utilizing the SPC (single point charge) water model. The system was neutralized by the addition of 4 Na^+ ions.

To reduce solvent fluctuations and eliminate any residual strain, energy minimization was performed using the steepest descent algorithm with a maximum of 50 000 steps and a step size of 0.01. Following this, equilibration was conducted at 300 K using the NVT and NPT ensembles. The LINCS algorithm was employed to constrain protein bond lengths. The velocity-Verlet method, along with the Macro model, was used for the Particle-Mesh Ewald (PME) approach to compute long-range electrostatic interactions, with a cutoff distance of 1.2 nm for short-range electrostatic forces.

Temperature control at 300 K was maintained using the Berendsen thermostat, and pressure was held at 1 atm with the Parrinello–Rahman method to avoid any system clashes. Trajectory analysis was carried out using VMD, yielding RMSD, RMSF, hydrogen bond count, and the radius of gyration.⁴⁴

4. In vitro studies

4.1 Anti-microbial study by zone of inhibition method

Antimicrobial activity refers to a substance's capability to prevent, kill, or inhibit the growth of microorganisms such as bacteria and fungi. The Kirby Bauer Disk Diffusion method was used to demonstrate this activity.⁴⁵

4.1.1 Antibacterial activity. The antibacterial activity of dibenzoxepinone derivative **7a** was studied against Gram-positive and Gram-negative bacteria by the agar plate diffusion method. Culture was obtained from Microbial Type Culture Collection, Chandigarh, India – Gram-positive *Bacillus subtilis* (MTCC 441) and Gram-negative *Escherichia coli* (MTCC 443). Bacterial stock cultures were maintained on nutrient agar slants at $4 \text{ }^\circ\text{C}$, and glycerol stocks were kept at $-80 \text{ }^\circ\text{C}$. Briefly, sterilized Nutrient Agar medium was poured into Petri dishes and solidified at room temperature. Using aseptic techniques, the agar plates were swabbed from an overnight bacterial primary culture to form a lawn. A sterile yellow tip (7 mm) was used to make the wells.

Compound **7a** was tested against Gram-positive *Bacillus subtilis* at the following six dilutions (0, 2.5 μg , 5 μg , 12.5 μg , 25 μg , and 50 μg). For *E. coli*, compound **7a** was prepared in three sets of dilutions (0, 25 μg , and 50 μg) for *E. coli*, prepared in DMSO of compound **7a**, and added to the well of the Petri plates. After 50 μL of each was added to the well, the plates were incubated at $37 \text{ }^\circ\text{C}$ for 24 h. The diameter of clear zones (mm) around each well was measured. Ampicillin (5 mg ml^{-1}) and DMSO were used as controls.⁴⁶

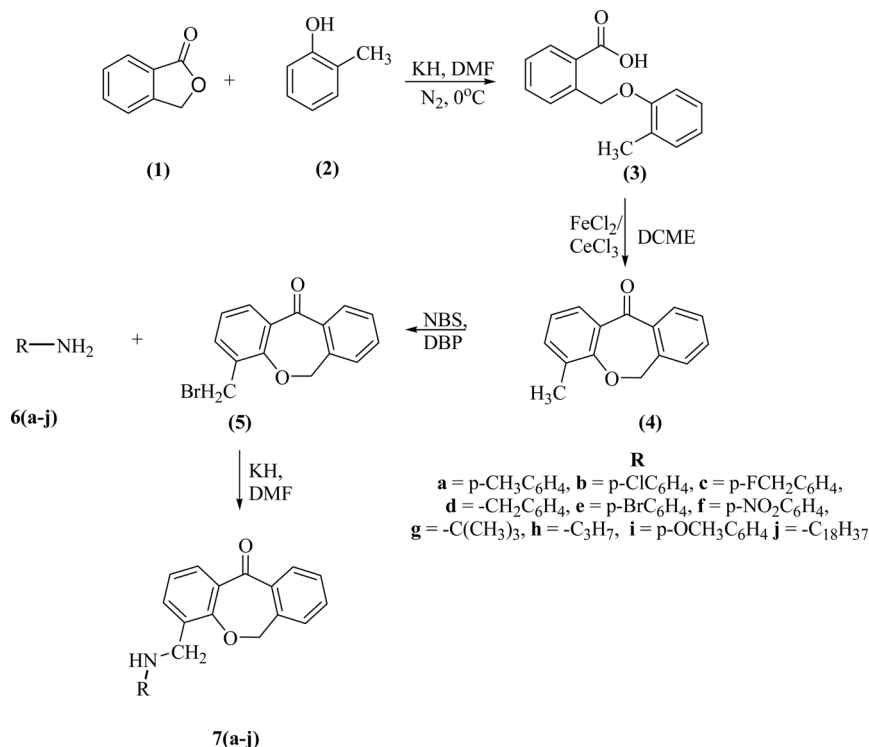
4.1.2 Antifungal activity. The antifungal activity was studied for the best binding compound **7a** from molecular docking with antifungal protein *candida albicans* (MTCC 183). The fungal strain was obtained from the Microbial Type Culture Collections, Chandigarh, India. Various concentrations of test samples (25 μg and 50 μg) were prepared in DMSO. Fluconazole (100 mg ml^{-1}) and DMSO were used as controls. Further, the plates were incubated at $30 \text{ }^\circ\text{C}$ for 20 hours. After incubation, the diameter of inhibition zones was measured in millimetres.⁴⁶

4.2 Antibacterial study by RMDA method

The antibacterial activity of the synthesized compounds was evaluated using the Resazurin Microtiter Assay (RMDA). The assay was performed under aseptic conditions using a 96-well microtiter plate. In the first row of the plate, 100 μL of each test compound (**7a–j**) was added at an initial concentration of $1024 \mu\text{g mL}^{-1}$ in DMSO. Subsequently, 100 μL of nutrient broth was added to each well. A twofold serial dilution was carried out along each column by transferring 100 μL from one well to the next, resulting in a final minimum concentration of $0.5 \mu\text{g mL}^{-1}$.⁴⁷

Following dilution, 10 μL of bacterial suspension adjusted to 0.5 McFarland standard (approximately $5 \times 10^6 \text{ CFU mL}^{-1}$) was introduced into each well. The bacterial strains tested were *Lacto bacillus rhamnosus* (MTCC1408), *Bacillus subtilis* (MTCC 441), and Gram-negative *Escherichia coli* (MTCC 443), each prepared separately. To prevent dehydration of the cultures, the





Scheme 2 Synthesis of dibenzoxepinone derivatives.

plates were sealed and gently wrapped with cling film. 30 μL of 5 mf per ml stock solution of ampicillin was injected as a positive control on each plate, and a negative control containing all reagents except the test compound was used.⁴⁸

The plates were incubated at 37 $^\circ\text{C}$ for 18–24 hours to allow bacterial growth. After incubation, 100 μL of 0.01% resazurin solution was added to each well as a viability indicator, and the plates were incubated for an additional 30 minutes. Antibacterial activity was assessed visually based on a color change in the wells. Ampicillin was used as the reference antibacterial agent.

4.3 ct-DNA study

Ct-DNA activity is a biochemical and biophysical phenomenon that encompasses the interaction of ct-DNA with ligands to

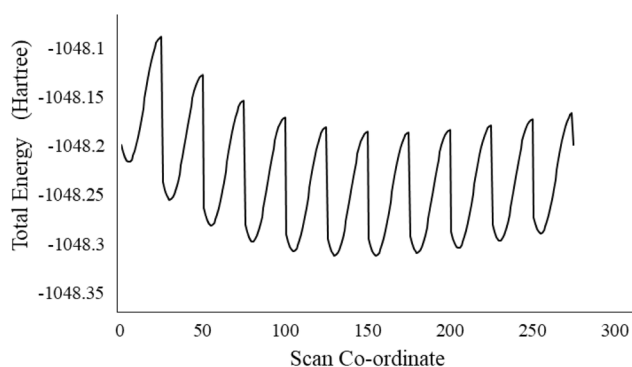
study the binding affinity. UV-visible absorption spectroscopy helps to identify the binding behavior of ct-DNA with compounds, and their interaction influences the absorbance property of the solution. A stock solution of ct-DNA (300 μM) was prepared in a Tris-HCl buffer solution containing 0.6 M HCl and 50 mM NaCl at pH 7.33. The UV absorbance ratio at 260 and 280 nm (A_{260}/A_{280}) was 1.9, confirming that the ct-DNA was free of protein contamination.⁴⁹ The concentration of ct-DNA was determined from its absorbance at 260 nm, using a molar extinction coefficient of 6600 cm^{-1} . A fixed volume (1 mL) of compounds **7a**, **7b**, and **7e** of concentration 10 μM was titrated with increasing concentrations (20–100 μM) of ct-DNA. The binding constant K_b was calculated by the Benesi-Hilderbrand equation.⁵⁰

$$\frac{A_0}{A - A_0} = \frac{\epsilon_G}{\epsilon_{H-G} - \epsilon_G} + \frac{\epsilon_G}{\epsilon_{H-G} - \epsilon_G} \frac{1}{K_b [\text{DNA}]}$$

where K_b is the binding constant, A and A_0 are the absorbance taken of ligands with ct-DNA at different concentrations and ligands without ct-DNA, respectively. ϵ_G and ϵ_{H-G} are the absorption coefficients taken of ligands with ct-DNA at different concentrations and ligands without ct-DNA, respectively. The binding energy was calculated by the ratio of intercept to the slope from the straight-line graph between $A_0/(A - A_0)$ vs. $1/\text{DNA}$.

5. Results and discussion

We successfully synthesized ten different derivatives of dibenzoxepin-11-one, the synthetic protocol includes four steps

Fig. 1 Potential energy scan of **7a**.

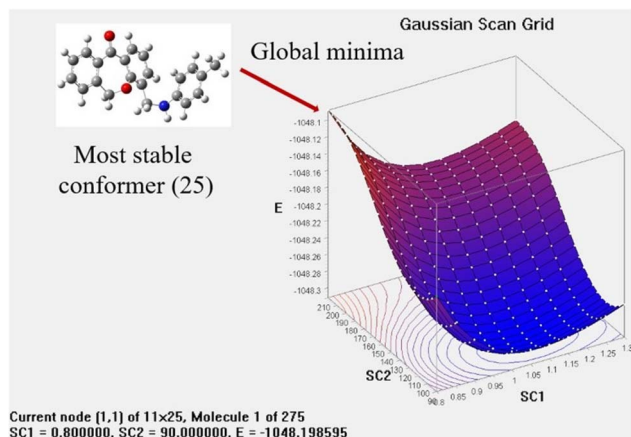


Fig. 2 Potential energy scan grid of 7a.

(Scheme 2). In the first step, the intermolecular cyclization of the C–O bond or Williamson ether synthesis reaction was performed between phthalide (1) and *o*-cresol (2) to form 2-((*o*-tolylloxy)methyl)benzoic acid (3). The synthesized compound was characterized by ^1H NMR and compared the peaks already given in the literature.²⁸ The peaks at 5.52 ppm and 2.34 ppm, which correspond to carbon–oxygen bond formation as O–CH₂ and –CH₃ group of tolyl moiety respectively, confirmed the formation of 3. In the next step, the intramolecular cyclization of compound (3) in the presence of Lewis acid (FeCl₂ or CeCl₃) and DCME was done and the product obtained as dibenzoxepin-11-one (4), its spectral proton NMR data was compared with the given literature data, the peaks of O–CH₂ at 5.52 ppm get shifted to the upfield range and observed at 5.22 ppm which confirmed that intramolecular cyclization has occurred. In the third step, the Wohl–Zeigler allylic bromination reaction of the methyl group present in tolyl ring was done.

Table 1 UV-visible absorption spectra details

Experimental		Theoretical/TD-DFT/6-31+G(d,p)		
λ_{cal} (nm)	Band gap (eV)	λ_{cal} (nm)	Band gap (eV)	<i>F</i> (frequency)
330.10	3.2146	332.44	3.7295	0.0367
373.56	2.9752	350.30	3.5393	0.0057
		457.29	2.7113	0.0039

The peak for methyl group peak in 4, which was initially at 2.34 ppm get shifted to the downfield at 3.22 ppm due to the substitution of a bromine atom in place of hydrogen in compound 5, validating the progress of the reaction. The formation of 5 was further confirmed by ^{13}C NMR and HRMS analysis. In the last step, the bromo group of 5 was treated with various substituted amines 6a–j. During this the CH₂–Br peak was replaced by CH₂–N– and the ^1H NMR showed a downfield shift of methylene protons at 4.45 ppm in compound 7a. In all other compounds from (7b–j), this peak was observed between 4.0 ppm to 5.0 ppm. In FTIR spectrum of 7a, showed a signal at 3390 cm⁻¹ frequency for the N–H bond, 1750 cm⁻¹ represents the carbonyl group, 1290 cm⁻¹ represents the N–CH₂, 990 cm⁻¹ represents C–O bond/ether linkage, and the other two peaks at 3010 cm⁻¹ and 1590 cm⁻¹ also verify the formation of compound 7a. Further, ^{13}C NMR and HRMS confirmed the formation of the desired product.

5.1 DFT study

5.1.1 Geometrical parameters. The potential Energy Scan (PES) method is highly recommended for defining the molecular stability through different conformational analyses. It is done for molecule 7a by the DFT method and using a B3LYP/6-31+G(d,p) basis set. This analysis has shown 275 conformers by rotating the most flexible NH group by changing the bond angle

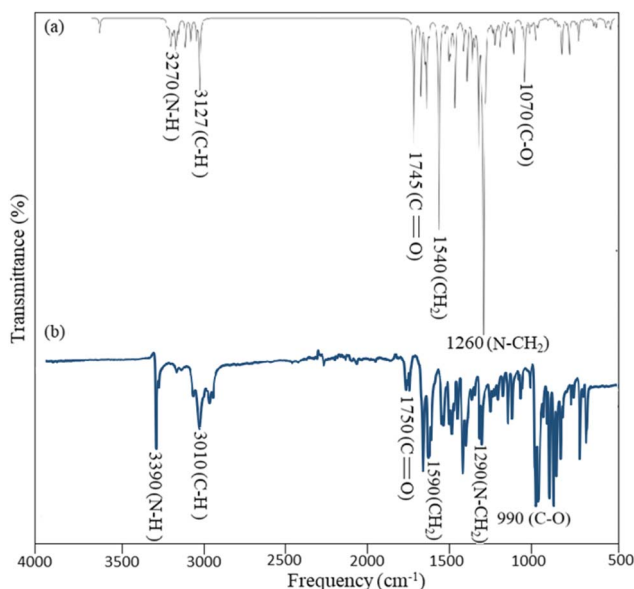


Fig. 3 FTIR Data (a) theoretical data (b) experimental data.

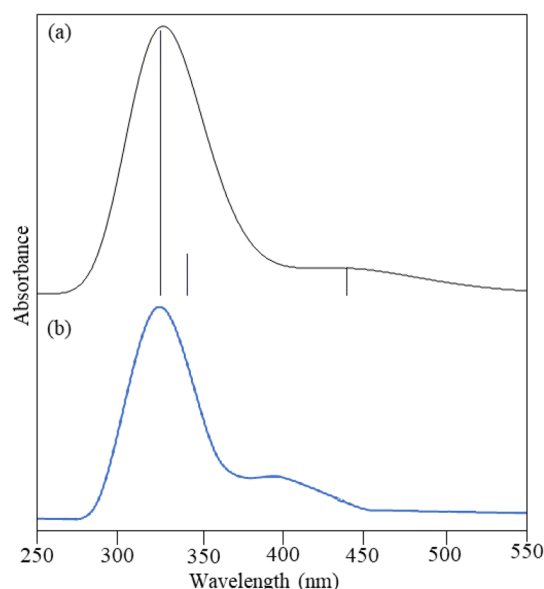


Fig. 4 UV-visible spectrum (a) theoretical (b) experimental.



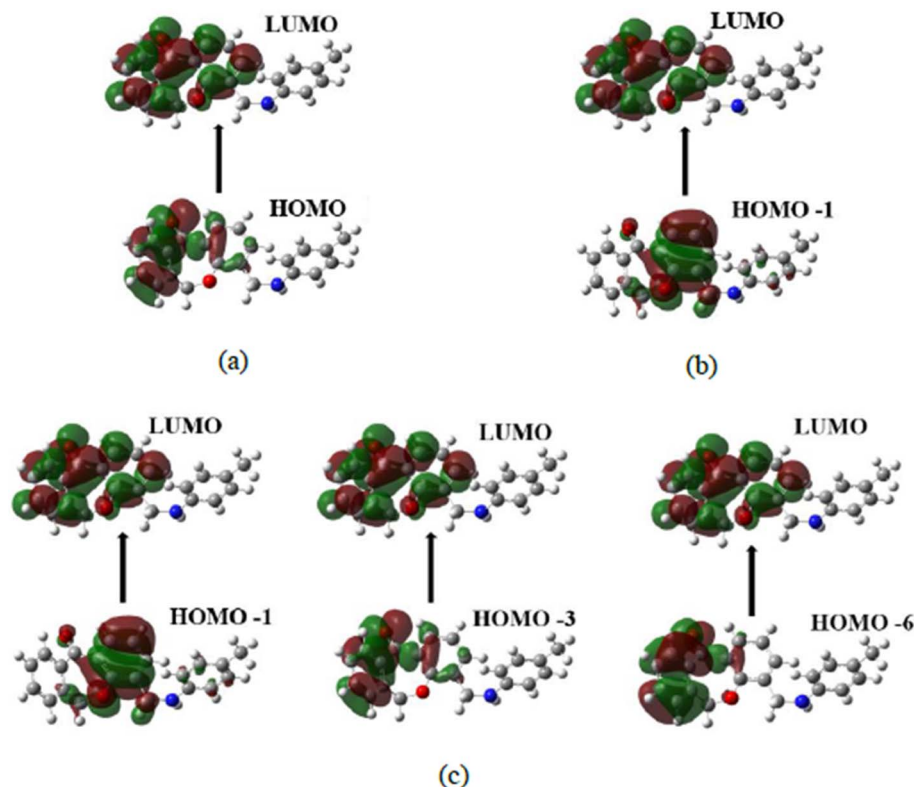


Fig. 5 Electronic transition orbitals in UV-visible (a) first excitation (b) second excitation (c) third excitation.

by 0.5° from 90° to its absolute angle and bond length by 0.05 from 0.8 to its standard bond length. Each conformation has different energy and stability as shown in Fig. 1. The lowest energy of the compound was found to be -1048.311765 hartree. The lowest energy conformer (Fig. 2) was used for further calculations such as FTIR and UV-visible.

5.1.2 Vibrational spectra analysis. FT-IR vibrational spectroscopy is a highly effective tool for the structural conformation of organic compounds. We have done theoretical and experimental FT-IR study for compound **7a**. Theoretical FTIR was calculated at B3LYP/6-31+G(d,p) basis set. Compound **7a** consists of 44 atoms and 126 vibrational modes, including three benzene rings, one oxepine ring with ketone group, one methyl group, one methylene group, and one N-H group. Oxygen and nitrogen atoms play an important role in structure elucidation. **7a** shows C-H, N-H, C-O, carbonyl, C-N, and C-C stretching vibrations within the range of different frequencies mentioned in Fig. 3. The current study found theoretical C-H stretching vibration at 3127 cm^{-1} , while the experimental FTIR band of

C-H stretching at 3010 cm^{-1} . N-H stretching vibration was observed at 3270 cm^{-1} at the B3LYP/6-31+G(d,p) basis set, and its experimental broadband was observed at 3390 cm^{-1} . Further carbonyl theoretical and experimental peak was found at 1745 cm^{-1} and 1750 cm^{-1} . In addition, C-N, C-O, and C-C stretching vibrations were observed at 1260, 1070, and 1540 cm^{-1} theoretically with slight variation in the experimental peaks at 1290, 990, and 1590 cm^{-1} respectively. There was a slight variation in theoretical and experimental FTIR peaks due to the model used having the best conformation in theoretical FTIR while experimentally we can't control the change in conformations.^{33,34}

5.1.3 Electronic properties. The theoretical UV-vis spectrum for compound **7a** was performed using TD-DFT/6-31+G(d,p) basis set by employing the solvent DMSO. An experimental UV-vis spectrum was also done in DMSO. The electronic transition orbitals are shown in Fig. 5. Experimental and theoretical calculations both measure absorption wavelength (λ) and excitation energy (E) during the electronic transition of an electron from the

Table 2 Amino acids present at the active binding site for antimicrobial activities

PDB:ID	Amino acids at the active site
1KZN	TYR119, TYR225, TYR107, TYR119, PHE339, PHE117, PHE240, PHE176, ILE111, ILE352, LEU451, LEU394, HIS227, CYS393, ASP110, ASN175, ASN392
1IYL	ARG76, ARG136, ARF186, ARG22, TYR26, TYR165, ILE90, ILE78, VAL71, ASP73, ASN46, PRO79, HIS95, GLU50, GLY77



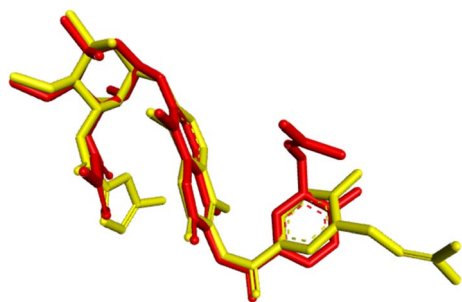


Fig. 6 Validation of the docking methodology by superimposing re-docked chlorobiocin (yellow color) with co-crystallized protein complex (red) with a RMSD: 1.54 Å.

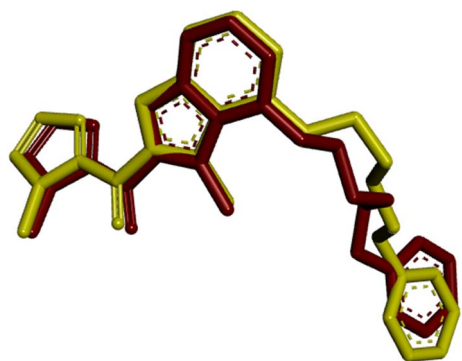


Fig. 7 Validation of the docking methodology by superimposing re-docked *N*-myristoyl transferase (yellow color) with co-crystallized protein complex (dark red) with a RMSD: 0.98 Å.

ground state to the excited state depicted in Table 1 and Fig. 4. The theoretical adsorption values were observed at 457.29, 350.30, and 332.44 nm associated with 0.0039, 0.0057, and 0.0367 oscillator frequencies. The first electronic transition was observed from HOMO > LUMO having a percentage coefficient of 99%. The second electronic transitions were found from HOMO-6 > LUMO, HOMO-3 > LUMO, and HOMO-1 > LUMO with a percentage coefficient of 10.33%, 83.26%, and 2.4%. The last electronic transition was observed from HOMO-1 > LUMO with 94.01%. The experimental UV showed a prominent absorbance at 330.10 nm and a smaller absorption near 373.56 nm.³⁵

5.2 Molecular docking

5.2.1 Active site of protein and validation of docking. The functionality of a protein is largely determined by the active binding site. To investigate and identify the active site residues involved in docking, the substrate chlorobiocin and *N*-myristoyl-transferase were utilized. This substrate was obtained from PDB:1D 1KZN and 1IYL, accessed *via* the RCSB PDB database. The active binding site, comprising the amino acid residues listed in Table 2, was analyzed. The same docking methodology was applied for validation. The re-docked complex and the co-crystallized complex of the antibacterial protein and antifungal protein was superimposed using Biovia Discovery Studio 2021 (version 21.2). Root-mean-square (RMSD) values of 1.54 Å and 0.98 Å were obtained, as illustrated in Fig. 6 and 7 demonstrating the high precision in the docking procedure.

5.2.2 Antibacterial molecular docking. All the synthesized compounds (7a–j) were docked with *E. coli* antibacterial PDB

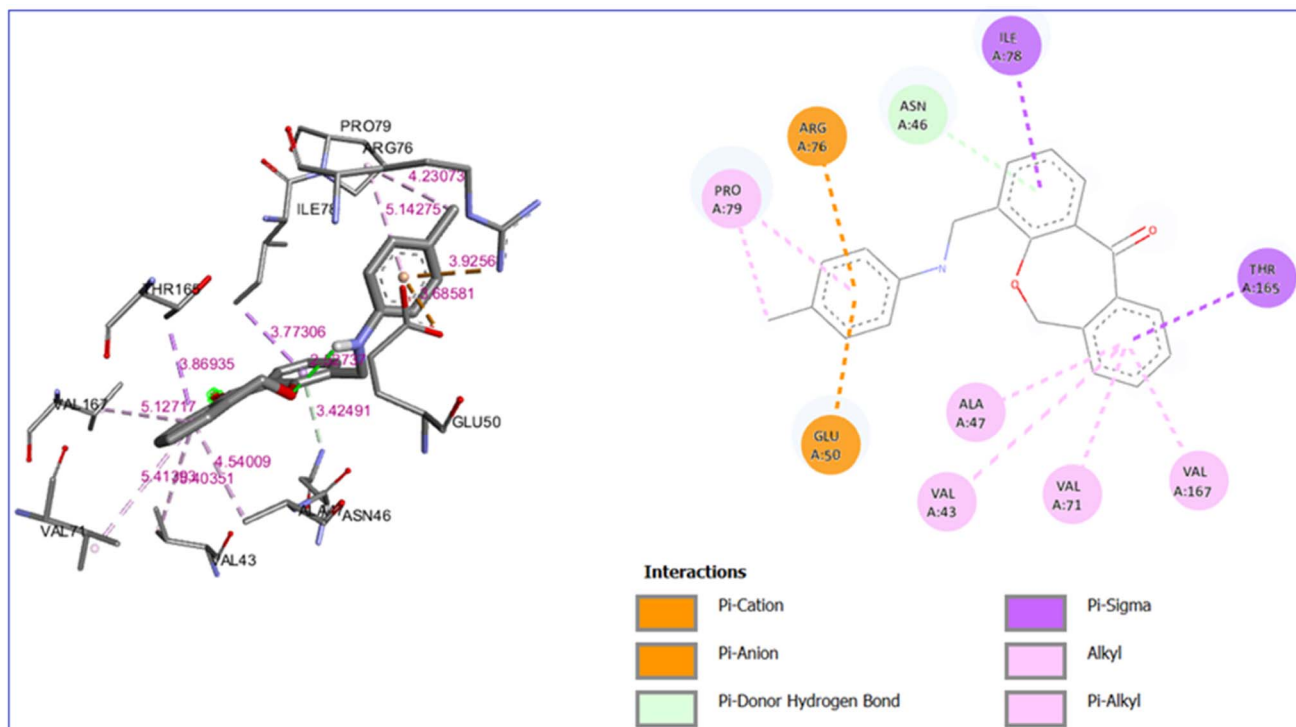


Fig. 8 3D and 2D interaction diagram of compound 7a with *E. coli* bacterial protein (PDB ID:1KZN).



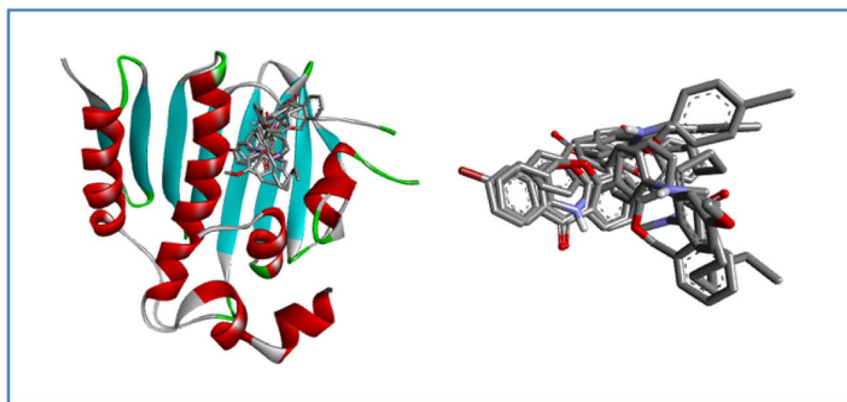


Fig. 9 Superimposition of docked ligand 7a–j conformations within the active site of the *E. coli* bacterial protein.

Id:1KZN to examine the interaction between the compounds and DNA gyrase protein (PDB Id:1KZN). Antibacterial protein DNA gyrase is critical for maintaining DNA supercoiling, which is vital for replication, transcription, and other cellular functions. Clorobiocin works by binding to the ATP-binding site of the GyrB subunit, blocking ATP hydrolysis a key step in the enzyme's activity of essential type II topoisomerase.⁵¹

This study revealed that all the compounds showed good binding interaction with different amino acids in the protein with different bonds. The binding energy range of the compounds with protein lies between -6.0 to -9.2 kcal mol⁻¹. The maximum binding energy -9.2 kcal mol⁻¹ was observed for compound 7a, as mentioned in Table S1,[†] which has a Pi-donor hydrogen bond with ASN 46, a Pi-sigma bond with ILE 78, and THR 165. Some of the interactions with bond length greater than 5 Å due to hydrophobic interactions but they still contribute to ligand

binding in long range binding interactions particularly between the charged residues and ligands. All other binding interactions are shown in Fig. 8. The interaction diagram of the remaining compounds was shown in Fig. S1[†] to S9.

Fig. 9 represents that all the ligands superimposing in the active site of the target after docking, it indicates a consistent binding mode and a well-defined binding pocket. This suggests that all derivatives interact with the same key residues, implying a common mechanism of action. Such consistency strengthens the reliability of the docking predictions and suggests that the ligands may exhibit similar biological activity.

5.2.3 Antifungal molecular docking. The molecular docking for all the compounds (7a–j) was done with *Candida albicans* protein *N*-myristoyl transferase (PDB ID:1IYL). *N*-Myristoyl transferase (NMT) is an essential enzyme that catalyzes the covalent attachment of a 14-carbon fatty acid, myristate, to the

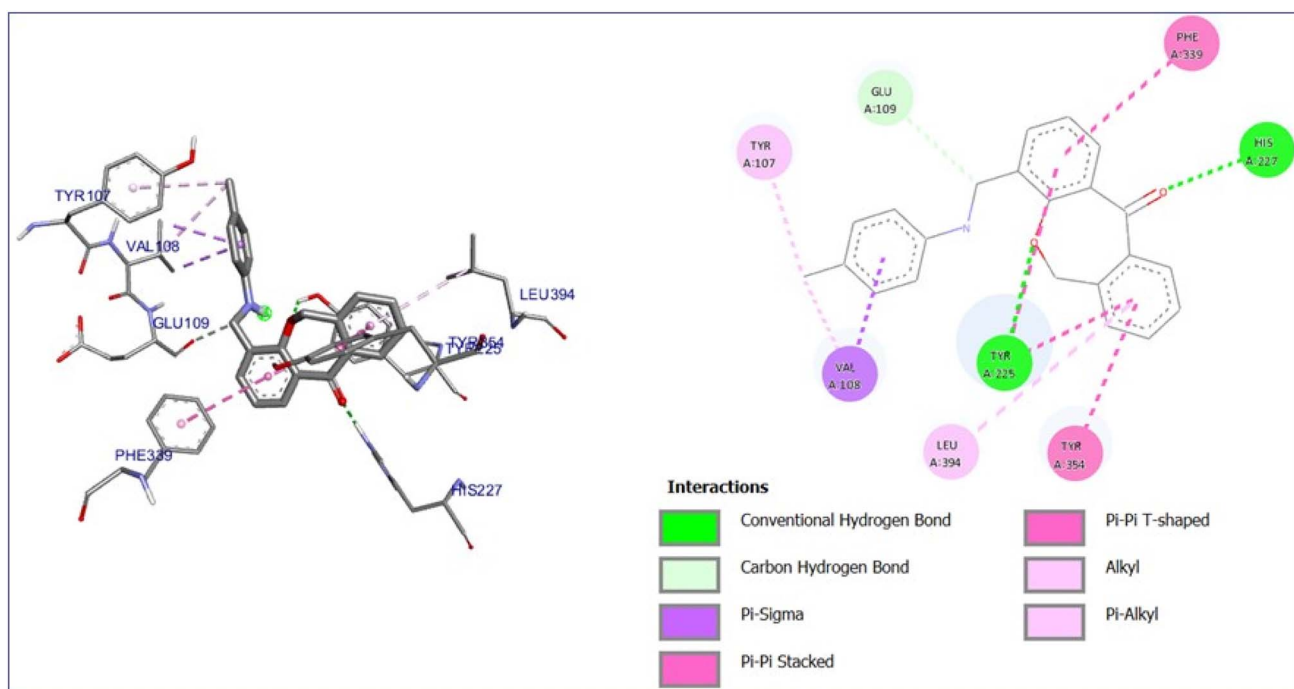


Fig. 10 3D and 2D interaction diagram of compound 7a with antifungal protein (PDB ID:1IYL).



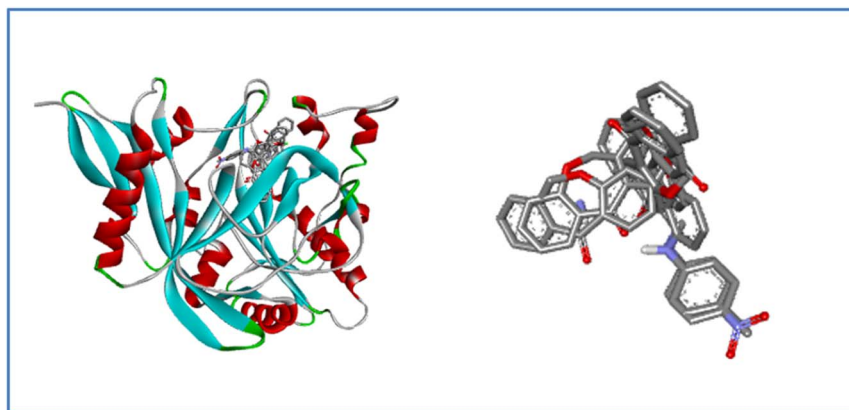


Fig. 11 Superimposition of docked ligand 7a–j conformations within the active site of the antifungal protein *N*-myristoyltransferase.

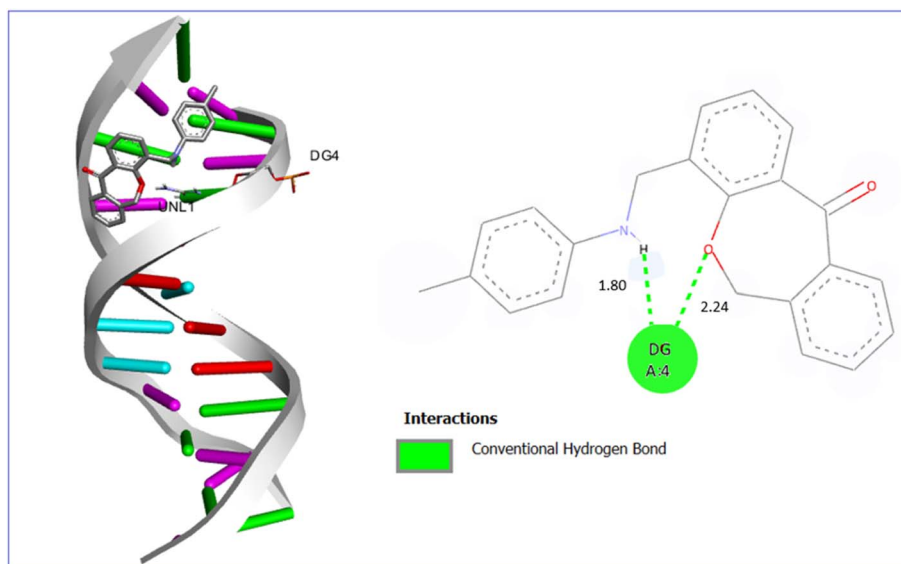


Fig. 12 3D and 2D interaction diagram of compound 7a with ct-DNA (PDB ID:1BNA).

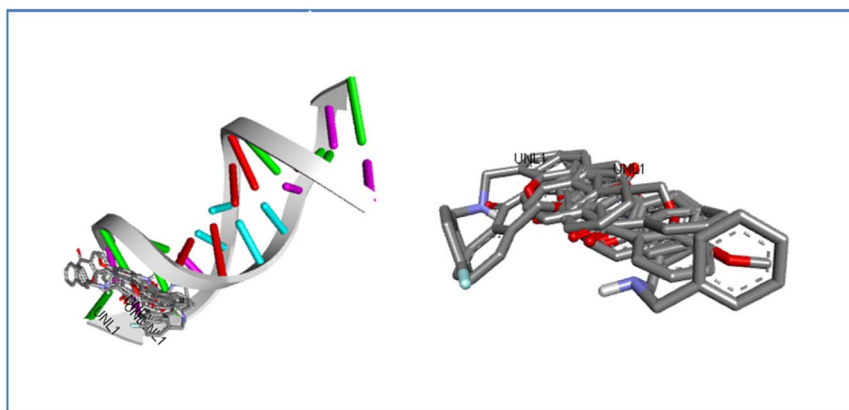


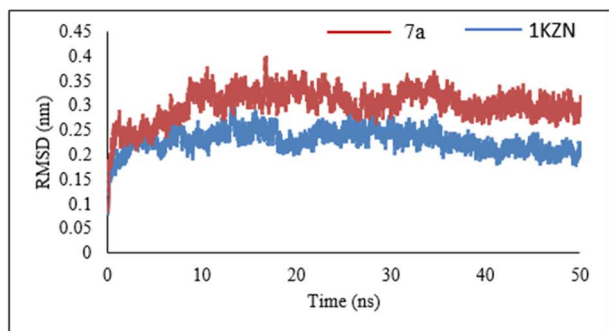
Fig. 13 Superimposition of docked ligand 7a–j conformations within the active site of DNA protein dodecamer.

N-terminal glycine residue of specific proteins in a co-translational and post-translational manner.

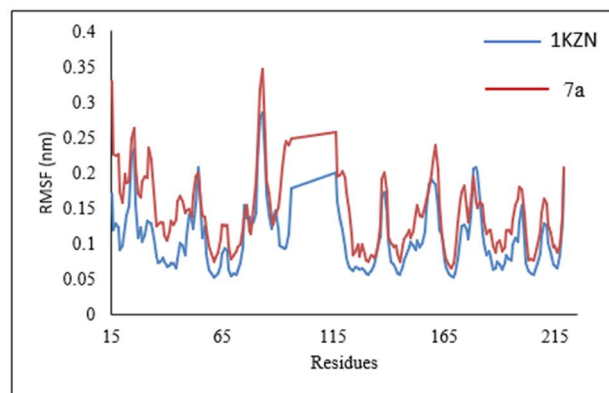
Its single-subunit enzyme facilitates the attachment of the fatty acid myristate from myristoyl-CoA to the N-terminal

glycine residue of various eukaryotic and viral proteins. PDB 1D:1IYL represents the crystal structure *N*-myristoyl transferase, which is an essential enzyme in ergosterol biosynthesis, and is a crucial component of fungal cell membranes. Inhibiting this

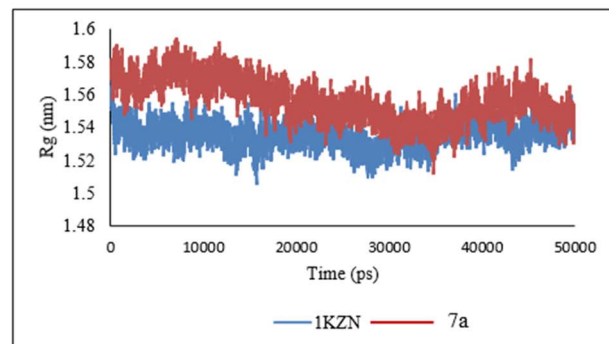




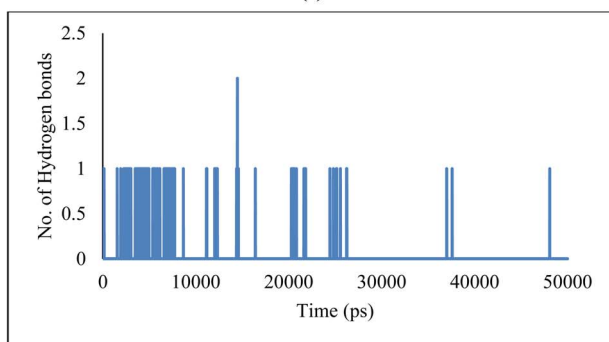
(a)



(b)

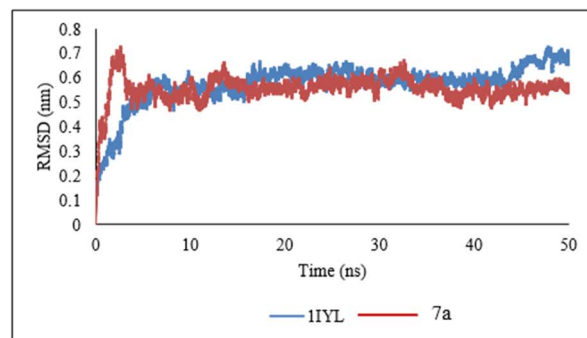


(c)

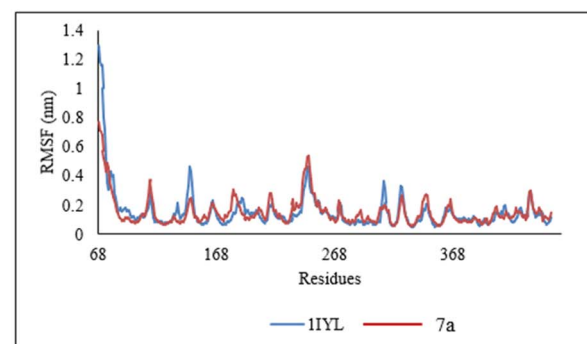


(d)

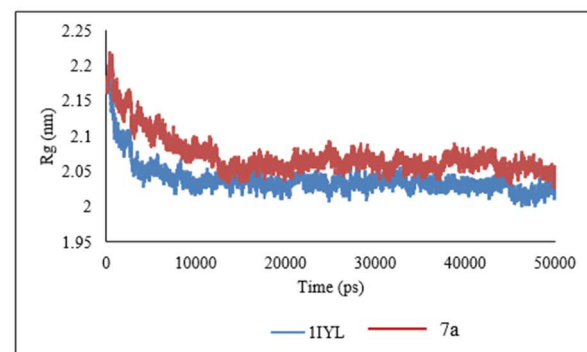
Fig. 14 (a) RMSD, (b) RMSF, (c) radius of gyration, and (d) hydrogen bonds of 7a ligand in complex with 1KZN protein.



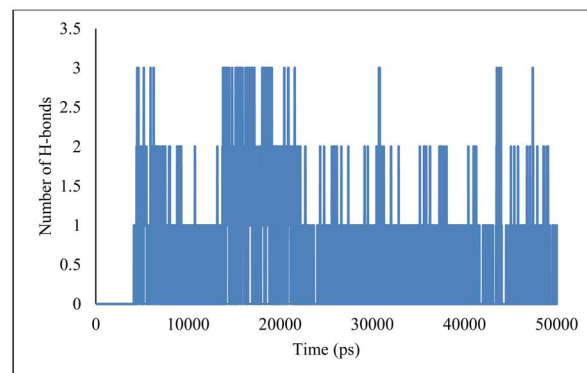
(a)



(b)



(c)



(d)

Fig. 15 (a) RMSD, (b) RMSF, (c) radius of gyration, and (d) hydrogen bonds of 7a ligand in complex with 1IYL protein.

enzyme can hinder ergosterol, weakening cell membrane integrity and ultimately causing cell death in fungi. The binding energy of the compounds with the protein falls in the range of

−8.0 to −11.0 kcal mol^{−1} noted in Table S1.† Affluence the capacity of cell death in fungi. 7a compound has the maximum binding energy (−11.0 kcal mol^{−1}) with some imperative bonds



such as conventional hydrogen bonds with TYR 225 and HIS 227, carbon–hydrogen bond with GLU 109, Pi-sigma bond with VAL 108, alkyl and Pi-alkyl bond with LEU 394 and TYR 107 as shown in Fig. 10. Interactions of compounds **7b–j** with protein are depicted in Fig. S10 to S18.†

Fig. 11 illustrates the superimposition of all ligands within the active site of the target after docking, demonstrating a consistent binding mode and a well-defined binding pocket. This indicates that all derivatives interact with the various amino acid residues, suggesting a similar mechanism of action. The high degree of overlap reinforces the reliability of the docking predictions and implies that the ligands may possess similar biological activity.

5.2.4 Molecular docking with ct-DNA. The molecular docking outcomes demonstrated that the synthesized derivative **7a** preferably binds with an AT-rich groove of the DNA sequence rather than to the terminal G-C. A DNA dodecamer is a short oligonucleotide of 12 base pairs, often employed as a model system in structural and biochemical studies of DNA. Ligand **7a** was complemented by the natural curvature of the DNA dodecamer, forming a groove combination mode as shown in Fig. 12.

Conventional hydrogen bonding played a significant role in the interaction of ligand **7a** with DNA through a maximum binding energy of $-8.1 \text{ kcal mol}^{-1}$. The conventional hydrogen bonds were formed between carboxylic acid and guanosine of A strand with a bond length of 2.24 Å and the NH group of the ligand and guanosine of A strand with a bond length of 1.80 Å as noted in the 2D diagram. All other ligands also showed groove binding with different bonding interactions and binding energies as mentioned in Table S1 and Fig. S19 to S27.†

Fig. 13 depicts the superimposition of all ligands within the target's active site after docking, highlighting a consistent binding mode and a well-defined binding pocket. This suggests that all derivatives interact with the same key residues, indicating a shared mechanism of action. The significant overlap enhances the credibility of the docking predictions and suggests that the ligands may exhibit similar biological activity. Additionally, the superimposition reinforces the strong affinity of the binding site for these ligands, making it a promising candidate for further drug optimization.

The docking results show that all the synthesized derivatives were showing good binding interaction with all the PDB IDs: 1KZN, 1IYL, AND 1BNA having range lie between -6.0 to $9.2 \text{ kcal mol}^{-1}$ for antibacterial target protein, -8.5 to $-11.0 \text{ kcal mol}^{-1}$ for antifungal target protein, and -5.3 to $-8.3 \text{ kcal mol}^{-1}$ for DNA gyrase, but compound **7a** has maximum binding energy with all target proteins that include different interactions like conventional hydrogen bond, carbon hydrogen bond, pi-sigma, and pi-alkyl, *etc.* Maximum bonding interactions of compound **7a** were observed with the target protein 1IYL, and 1BNA shows the best binding with it and good biological activity.

5.3 ADME and physicochemical parameters

For drug development, synthesized derivatives should have a good ADME profile. 'Lipinski's rule of five' parameters such as

Table 3 Diameter of the zone of inhibition for antimicrobial activity of compound **7a**

Concentration (μg)	Diameter of zone of inhibition (mm)		
	<i>E. coli</i>	<i>Bacillus subtilis</i>	<i>Candida albicans</i>
5	—	—	—
12.5	—	12	—
25	16	15	15
50	17	17	18
Ampicillin ^a	20	24	—
Fluconazole ^a	—	—	15

^a Positive control.

(i) MW under 500, (ii) no. of hydrogen bond less than 5, (iii) no of hydrogen bond acceptors less than 10, (iv) log *P* value less than 5, (v) total polar surface area (TPSA) should not be greater than 140 \AA^2 , indicates that the molecule is likely to be an orally active drug or not. Additionally, one violation is acceptable. All the molecules obey Lipinski's rule except **7b** and **7c**, they both have one violation. Other ADME parameters like blood–brain barrier (BBB), CaCo₂, HIA, and protein plasma binding lie in the range of active drug noted in Table S3,† which means that compounds **7a–j** behave as orally active drug.

A bioactivity score of less than -5.0 suggests the compound is inactive, a score between -5.0 and 0.0 indicates slight activity, and a score greater than 0.0 signifies high activity. All synthesized derivatives fall in the range and exhibit good bioactivity scores in Table S4.†

5.4 MD simulation

The dynamic stability of the optimal dibenzoxepine complex with the antibacterial protein and antifungal protein (PDB ID: 1KZN and 1IYL) was assessed through MD simulation using Gromacs. Ligand topology was generated *via* the free online ATB server, and the GROMOS96 force field was applied to the simulated complex. The dibenzoxepine–protein complex was initially positioned within a cubic simulation box, followed by energy minimization in a solvated system. After energy minimization, MD simulations were conducted for 50 ns under constant conditions of 300 K temperature and 1 atm pressure.

5.4.1 Molecular dynamics (MD) simulation study of **7a** in complex with antibacterial protein

5.4.1.1 Root mean square deviation (RMSD). The interaction between the backbone atoms of the native 1KZN protein and its complex with **7a** was analyzed using the Root Mean Square Deviation (RMSD) method. A stable RMSD pattern was observed for 50 ns. However, variations in RMSD values were noted,

Table 4 MIC values of synthesized derivatives against different bacterial strains

MIC values ($\mu\text{g ml}^{-1}$)	7a	7b	7c	7d	7e	7f	7g	7h	7i	7j
<i>L. rhamnosus</i>	8	8	8	16	64	8	32	32	8	128
<i>B. subtilis</i>	16	16	16	32	16	128	128	16	16	256
<i>E. coli</i>	8	16	8	16	16	32	32	64	16	128



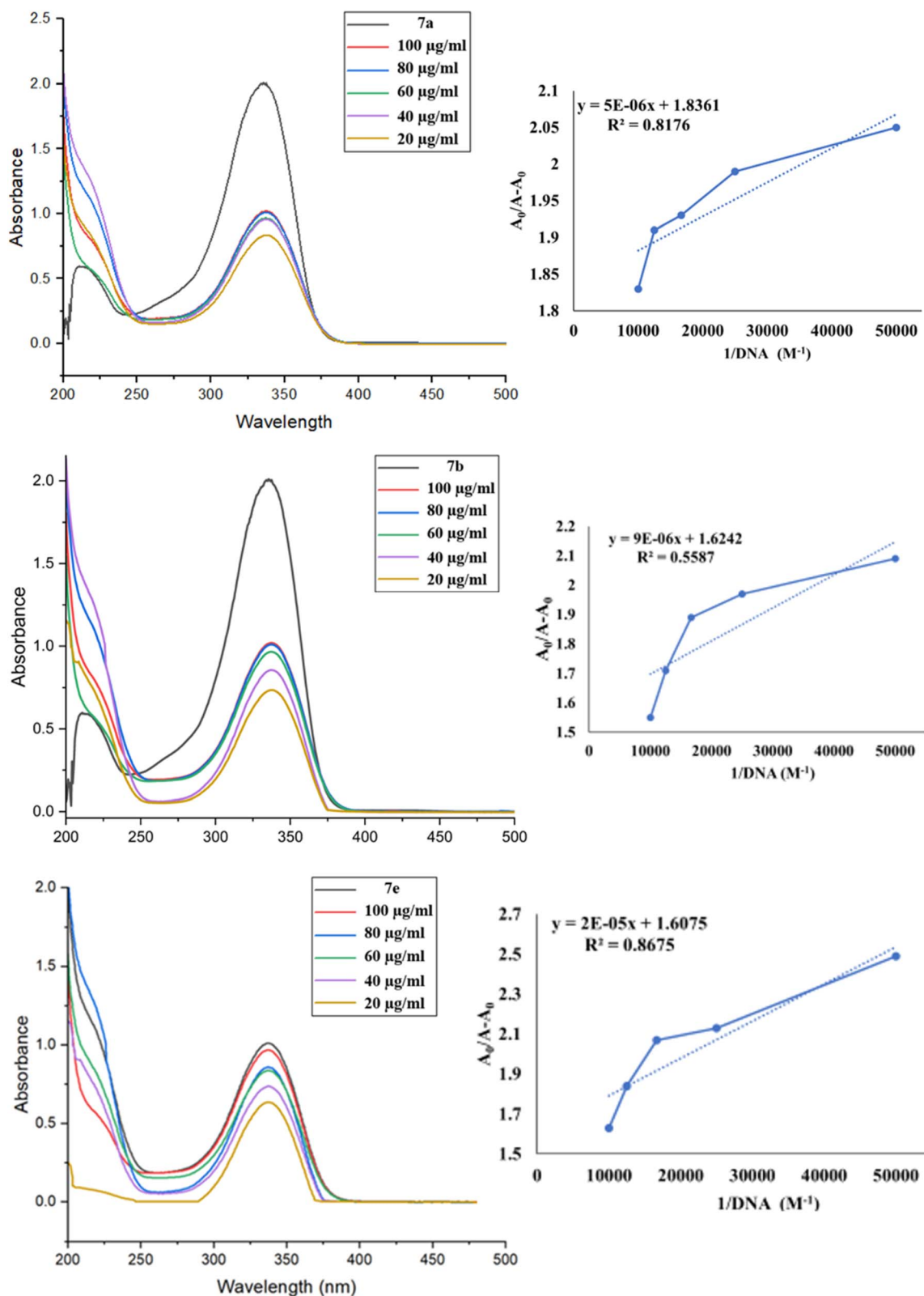


Fig. 16 UV-Vis spectral changes were observed in 7a, 7b, and 7e at a concentration of 10 μM in 50 mM Tris-HCl/NaCl buffer (pH = 7.35) at 25 $^\circ\text{C}$, as the ct-DNA concentration increased from (20–100 μM). The arrow indicates a decrease in absorbance as the ct-DNA concentration increases.

ranging from 0.1 nm to 0.39 nm for the native 1KZN protein (Fig. 14a). These minor variations reflect the stability of the protein-ligand complex.

5.4.1.2 Root mean square fluctuation (RMSF). The residue-wise variations were analyzed using Root Mean Square Fluctuation (RMSF). As shown in Fig. 14b, the 7a-protein complex



exhibited fluctuations comparable to those of the native 1KZN structure, suggesting that the complex maintained significant stability due to ligand interactions.

5.4.1.3 Radius of gyration (R_g). The structural compactness of the protein was assessed using the Radius of Gyration (R_g). A consistent pattern was observed, with R_g values ranging from 1.51 nm to 1.61 nm (Fig. 14c) when comparing the native 1KZN protein with its ligand-bound complex. These results indicate the formation of a stable complex characterized by high structural compactness.

5.4.1.4 Hydrogen bonds. The analysis of antibacterial activity demonstrated a consistent and significant number of hydrogen bonds within the 7a–1KZN complex throughout the 50 ns MD simulation (Fig. 14d). The presence of these hydrogen bonds confirmed the structural integrity of the protein, strong protein–ligand interactions, and overall stability of the complex.

5.4.2 Molecular dynamics (MD) simulation study of 7a in complex with antifungal protein

5.4.2.1 Root mean square deviation (RMSD). The interaction between the backbone atoms of the native 1IYL protein and its complex with 7a was evaluated using the Root Mean Square Deviation (RMSD) method. A stable RMSD pattern was observed over the 50 ns simulation period, with variations ranging from 0.1 nm to 0.34 nm for the native IYL protein (Fig. 15a). These minor deviations highlight the stability of the protein–ligand complex.

5.4.2.2 Root mean square fluctuation (RMSF). Residue-wise variations were analyzed using the Root Mean Square Fluctuation (RMSF) method. As depicted in Fig. 15b, the 7a–protein complex displayed fluctuations similar to those of the native 1IYL structure, indicating significant stability of the complex due to ligand interactions.

5.4.2.3 Radius of gyration (R_g). The structural compactness of the protein was analyzed using the Radius of Gyration (R_g). A consistent trend was observed, with R_g values ranging from 2.01 nm to 2.75 nm (Fig. 15c) for both the native 1IYL protein and its ligand-bound complex. These findings confirm the formation of a stable complex with high structural compactness.

5.4.2.4 Hydrogen bonds. The evaluation of antibacterial activity revealed a stable and substantial number of hydrogen bonds within the 7a–1IYL complex during the 50 ns MD simulation (Fig. 15d). These hydrogen bonds underscore the structural integrity of the protein, robust protein–ligand interactions, and overall stability of the complex.

5.5 Antimicrobial activity

5.5.1 Zone of inhibition method. The findings from the antibacterial and antifungal activity assay revealed that compound 7a demonstrated differing levels of inhibition against Gram-positive *B. subtilis*, Gram-negative *E. coli*, and *C. albicans* strains, as shown in Fig. S28.† The assessment included measuring the sizes of the inhibitory zones, encompassing the diameter of the disk, to gauge the compound's efficacy in hindering bacterial and fungus growth.

Moreover, the zones of inhibition results revealed the compound's potential to inhibit the growth of bacteria and fungus strains. Thus, emphasizing that the synthesized compound 7a is a bioactive compound with significant anti-microbial potential leading to growth inhibition. The diameter of the zone of inhibition increases as the concentration of compound 7a increases (Table 3).

5.5.2 RMDA method. As the compound 7a showed the good zone of inhibition for different bacterial strains, further all the synthesized derivatives were tested against three bacterial strains (*Lacto bacillus rhamnosus* MTCC1408, *Bacillus subtilis* MTCC 441, and *E.coli* MTCC 443) for MIC evaluation. The outcomes of the antibacterial evaluations demonstrated that compounds 7a, 7b, 7c, and 7i exhibited lowest MIC value against both the Gram-positive bacterial strains *Lacto bacillus rhamnosus* MTCC1408 and *Bacillus subtilis* MTCC 441. However, 7a and 7c have lowest MIC value for Gram negative strain *E. coli* MTCC 443 (Table 4 and Fig. S29†). Resazurin (7-hydroxy-3H-phenoxazin-3-one-10-oxide), a blue dye with slight fluorescence, was utilized as an oxidation-reduction indicator in the assay. This dye is commonly used in cell viability assessments for both microbial and mammalian cells. A positive antibacterial response was indicated by a color change from blue or purple to pink, resulting from bacterial metabolic activity.

5.6 ct-DNA binding activity

5.6.1 UV-visible absorption. The UV-visible absorption method is valuable for the qualitative and quantitative analysis of ct-DNA binding with synthesized dibenzoxepinones. This method often reveals the change in absorption, which can manifest as hyperchromic and hypochromic, along with shifts in the maximum absorption wavelength, indicating blue and red shifts. In the present study, the synthesized compounds 7a, 7b, and 7e were chosen for study to bind with ct-DNA. The UV spectrum of compounds was recorded, showing a peak at 330 nm absorbance and was attributed to the intra-ligand π – π^* electron transition within the C–N system. The gradual addition of ct-DNA, leading to a hypochromic shift, and the absence of the red or blue shift in the binding of ct-DNA with ligands was groove binding (Fig. 16).

The intrinsic binding constant (K_b) was evaluated from intercept by slope ratio from the equivalent double reciprocal graph of $A_0/A - A_0$ against $1/[DNA]$ mentioned in Table 5. The hypochromic effects of compounds with ct-DNA and the K_b values confirmed their stable interaction.

The Gibbs free energy (ΔG) of the compounds (7a, 7b, 7e)/ctDNA complex can account for the complex's stability was assessed when ct-DNA was introduced into the solution. The

Table 5 Binding constants (K_b , M^{-1}), and Gibbs free energy (ΔG , $kJ mol^{-1}$) of compounds

Compounds	7a	7b	7e
Binding constant (K_b)	3.61×10^5	1.80×10^5	8.03×10^4
Gibbs free energy (ΔG)	–31.70	–29.98	–27.98



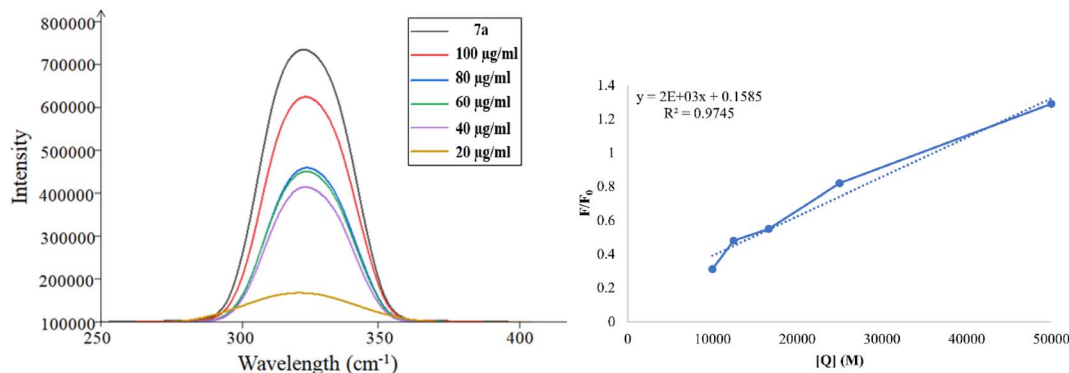


Fig. 17 Fluorescence emission spectra of **7a** (10 μM) with an increasing concentration of ct-DNA (0–100 μM). The inset shows the Stern–Volmer constant (K_{sv}). The arrow shows a decrease in intensity with an increase in ct-DNA concentration.

equation below was used to calculate the free energy of the system utilizing the relevant parameters:

$$\Delta G = -RT \ln(K_b)$$

The analysis of the Gibbs free energy cited in Table 5 for the complexes revealed that the binding of compound **7a** with ct-DNA was thermodynamically more stable.

5.6.2 Fluorescence quenching studies of compound 7a/ct-DNA. The UV study indicated that **7a** was the best binder of ct-DNA, therefore further study has been performed for UV Fluorescence quenching. The fluorescence quenching study of **7a** was analyzed to investigate its binding interaction with DNA, given that DNA itself exhibits weak natural fluorescence. Fig. 17 presents the fluorescence emission spectrum resulting from the titration of **7a** with ct-DNA using the excitation wavelength of 330 nm. The observed decrease in peak intensities upon the addition of ct-DNA intensities suggests the formation of a stable complex and enhanced interaction between ct-DNA and **7a**.

Fluorescence quenching is a process where the fluorescence intensity of a substance diminishes, typically occurring due to various molecular interactions such as ground state complex formation, excited state reactions, and molecular rearrangement. The effectiveness of fluorescence quenching can be assessed using the Stern–Volmer equation to determine the Stern–Volmer quenching constant (K_{sv}):

$$\frac{F_0}{F} = 1 + K_{\text{sv}}[Q]$$

In this context, F_0 and F represent the fluorescence intensities in the absence and presence of the quencher, respectively while $[Q]$ denotes the quencher concentration. The Stern–Volmer quenching constant (K_{sv}) is obtained from the slope of the F_0/F vs. [ct-DNA] plot. For compound **7a**, the K_{sv} value was determined to be $2.0 \times 10^3 \text{ M}^{-1}$, suggesting a non-intercalative binding mode, as this value is lower than those typically associated with intercalators. The distinction between static and dynamic quenching can be determined by examining the

linearity of the Stern–Volmer plot and applying the relevant equation.

$$K_q = \frac{K_{\text{sv}}}{\tau^0}$$

In this equation, K_q represents the biomolecular quenching rate constant and τ^0 is the biomolecule's fluorescence lifetime of the biomolecule in the quencher's absence. With τ^0 at 10^{-8} s , K_q was calculated to be $2.0 \times 10^{11} \text{ M}^{-1} \text{ s}^{-1}$. A high K_q value suggests that the quenching occurs *via* static quenching through complex formation rather than dynamic quenching. Hence, compound **7a** can bind with ct-DNA at the groove binding site.

Conclusion

Ten novel derivatives of dibenzoxepine-11-one were synthesized and demonstrated the ability to bind effectively with key biological targets, including bacterial DNA gyrase (PDB ID:1KZN, *E. coli*), *N*-myristoyltransferase (PDB ID:1IYL, *C. albicans*), and the DNA dodecamer (PDB ID:1BNA, ct-DNA). Molecular docking studies revealed favorable binding energies across all targets, with compound **7a** exhibiting the highest binding affinities of $-9.2 \text{ kcal mol}^{-1}$ with *E. coli*, $-11.0 \text{ kcal mol}^{-1}$ with *C. albicans*, and $-8.1 \text{ kcal mol}^{-1}$ with ct-DNA. The *in vitro* antimicrobial activity was done compound **7a** against *B. subtilis*, *C. albicans*, and *E. coli*. At a concentration of 50 μg , compound **7a** showed the highest zone of inhibition, with diameters of 17 mm against the bacterial strains and 18 mm against the fungal strain comparable to the standard antimicrobial agents Ampicillin and Fluconazole. These results were further validated for all the compounds by RMDA method to find MIC values against Gram-positive strains (*B. subtilis*, *L. rhamnosus*) and a Gram-negative strain (*E. coli*). Compounds **7a**, **7b**, **7c**, and **7i** demonstrated notable antibacterial potency, exhibiting lowest minimum inhibitory concentration (MIC) values for the Gram-positive strains, however, **7a** & **7c** have lowest MIC values for both Gram-positive and negative strains. Additionally, DNA-binding studies with calf thymus DNA on compounds **7a**, **7b**, **7c**, again confirmed that compound **7a** was the most potent groove



binder, with a binding constant (K_b) of $3.61 \times 10^5 \text{ M}^{-1}$ and a Gibbs free energy of $-31.70 \text{ kJ mol}^{-1}$. Overall, compound **7a** emerged as the most promising candidate, showing superior performance across all *in vitro* evaluations, which was further validated by *in silico* approaches, including DFT calculations and molecular dynamics simulations.

Abbreviations

DFT	Density functional theory
ct-DNA	Calf thymus deoxyribose nucleic acid
PSA	Polar surface area
UV	Ultra-violet
BBB	Blood-brain barrier

Data availability

The authors confirm that the supporting findings of this study are available within the article and are ESI.†

Author contributions

Dr Leena Khanna and Prof Pankaj Khanna: conceptualization of idea, supervision. Shilpa Yadav, Asmita Singh: literature search and primary draft and drawing of figures and tables. Shilpa Yadav, Priyanshu, Pratibha Chanana: performed *in vitro* experiments. Shilpa Yadav & Mansi: DFT study, execution of molecular docking and simulation of ligands. All authors reviewed the manuscript.

Conflicts of interest

The authors state no conflict of interest.

Acknowledgements

The authors would like to thank the Faculty Research Grant Scheme (FRGS 2024-25), Guru Gobind Singh Indraprastha University, Dwarka, New Delhi, for the financial support of this project. Shilpa Yadav, Asmita Singh and Mansi are thankful to Guru Gobind Singh Indraprastha University, Dwarka, New Delhi, for providing STRF.

References

- K. Zimmermann, P. C. Waldmeier and W. G. Tatton, Dibenzoxepines as Treatments for Neurodegenerative Diseases, *Pure Appl. Chem.*, 1999, **71**(11), 2039–2046, DOI: [10.1351/pac199971112039](https://doi.org/10.1351/pac199971112039).
- C. Limban and M. C. Chifriuc, Antibacterial Activity of New Dibenzoxepinone Oximes with Fluorine and Trifluoromethyl Group Substituents, *Int. J. Mol. Sci.*, 2011, **12**(10), 6432–6444, DOI: [10.3390/ijms12106432](https://doi.org/10.3390/ijms12106432).
- F. Naporra, S. Gobleider, H. J. Wittmann, J. Spindler, M. Bodensteiner, G. Bernhardt, H. Hübner, P. Gmeiner, S. Elz and A. Strasser, Dibenzob[b,f][1,4]Oxazepines and Dibenzob[b,e]Oxepines: Influence of the Chlorine Substitution Pattern on the Pharmacology at the H1R, H4R, 5-HT2AR and Other Selected GPCRs, *Pharmacol. Res.*, 2016, **113**, 610–625, DOI: [10.1016/j.phrs.2016.09.042](https://doi.org/10.1016/j.phrs.2016.09.042).
- W. F. Yeung, K. F. Chung, K. P. Yung and T. H. Y. Ng, Doxepin for Insomnia: A Systematic Review of Randomized Placebo-Controlled Trials, *Sleep Med. Rev.*, 2015, **19**, 75–83, DOI: [10.1016/j.smrv.2014.06.001](https://doi.org/10.1016/j.smrv.2014.06.001).
- J. Katwala, A. K. Kumar, J. J. Sejpal, M. Terrence and M. Mishra, Therapeutic Rationale for Low Dose Doxepin in Insomnia Patients, *Asian Pacific J. Trop. Dis.*, 2013, **3**(4), 331–336, DOI: [10.1016/S2222-1808\(13\)60080-8](https://doi.org/10.1016/S2222-1808(13)60080-8).
- H. Krawczyk, Dibenzob[b,f]Oxepine Molecules Used in Biological Systems and Medicine, *Int. J. Mol. Sci.*, 2023, **24**(15), 12066, DOI: [10.3390/ijms241512066](https://doi.org/10.3390/ijms241512066).
- B. Sadek, C. Limban, C. E. Stecoza and S. Elz, Synthesis and Antimicrobial Evaluation of Dibenzob[b,e]Oxepin-11(6H)-One O-Benzoyloxime Derivatives, *Sci. Pharm.*, 2011, **79**(4), 749–761, DOI: [10.3797/scipharm.1107-02](https://doi.org/10.3797/scipharm.1107-02).
- C. X. Liu, Z. X. Lin and A. M. Zhou, Design, Synthesis, Cytotoxicities and DNA Cleavage Activities of Dibenzoxepine and Isoquinoline Derivatives Starting from Dehydroabietylamine, *J. Asian Nat. Prod. Res.*, 2016, **18**(12), 1169–1177, DOI: [10.1080/10286020.2016.1232251](https://doi.org/10.1080/10286020.2016.1232251).
- D. Garbicz, P. Tobiasz, F. Borys, T. Pilżys, M. Marcinkowski, M. Poterała, E. Grzesiuk and H. Krawczyk, The Stilbene and Dibenzob[b,f]Oxepine Derivatives as Anticancer Compounds, *Biomed. Pharmacother.*, 2020, **123**(20), 109781, DOI: [10.1016/j.biopha.2019.109781](https://doi.org/10.1016/j.biopha.2019.109781).
- P. Khanna, D. Gupta, S. Yadav and L. Khanna, Hydrotrope Assisted Green Synthesis of Dicoumarols and *in Silico* and *in Vitro* Antibacterial, Antioxidant and Xanthine Oxidase Inhibition Studies, *J. Biomol. Struct. Dyn.*, 2023, **41**(19), 9651–9665, DOI: [10.1080/07391102.2022.2145368](https://doi.org/10.1080/07391102.2022.2145368).
- S. Yadav, N. Misra, P. Khanna and L. Khanna, Novel 10,11-Dihydro-5H-Dibenzob[b,f]Azepine Triazoles Hybrids: Synthesis, *in Vitro* Antioxidant Activity and Xanthine Oxidase Inhibition and Computational Study, *J. Mol. Struct.*, 2024, **1312**(P1), 138639, DOI: [10.1016/j.molstruc.2024.138639](https://doi.org/10.1016/j.molstruc.2024.138639).
- L. Khanna, S. Singhal, S. C. Jain and P. Khanna, Spiro-Indole-Coumarin Hybrids: Synthesis, ADME, DFT, NBO Studies and *In Silico* Screening through Molecular Docking on DNA G-Quadruplex, *ChemistrySelect*, 2020, **5**(11), 3420–3433, DOI: [10.1002/slct.201904783](https://doi.org/10.1002/slct.201904783).
- S. Yadav, N. Misra, P. Khanna and K. Batra, A DFT Study on Diels-Alder Reaction of Dibenzazepine and 2,5-Dimethylfuran Using Different Solvents and Temperature Conditions A DFT Study on Diels-Alder Reaction of Dibenzazepine And, *Polycycl. Aromat. Compd.*, 2022, 1–12, DOI: [10.1080/10406638.2022.2056622](https://doi.org/10.1080/10406638.2022.2056622).
- P. Khanna, S. Yadav, A. Singh and L. Khanna, Inclusion Complexes of Novel Formyl Chromone Schiff Bases with β -Cyclodextrin: Synthesis, Characterization, DNA Binding Studies and *in-Vitro* Release Study, *Carbohydr. Polym.*,



- 2025, 347(2024), 122667, DOI: [10.1016/j.carbpol.2024.122667](https://doi.org/10.1016/j.carbpol.2024.122667).
- 15 S. Sevvanthi, S. Muthu, M. Raja, S. Aayisha and S. P. E. S. Janani, Molecular Structure, Spectroscopic (FT-IR, FT-Raman), Electronic (UV-Vis, HOMO-LUMO), Quantum Chemical and Biological (Docking) Studies on a Potent Membrane Permeable Inhibitor: Dibenzoxepine Derivative, *Heliyon*, 2020, 6(8), e04724, DOI: [10.1016/j.heliyon.2020.e04724](https://doi.org/10.1016/j.heliyon.2020.e04724).
- 16 A. Manwal, P. Mekoung, A. Malloum, M. Govindarajan, R. N. Mballa, I. Patouossa, A. Abouem A Zintchem, C. P. N. Nansu and I. N. Mbouombouo, Spectroscopic Properties (FT-IR, NMR and UV) and DFT Studies of Amodiaquine, *Heliyon*, 2023, 9(12), e30645, DOI: [10.1016/j.heliyon.2023.e22187](https://doi.org/10.1016/j.heliyon.2023.e22187).
- 17 S. Murugavel, C. S. Jacob Prasanna Stephen, R. Subashini and D. AnanthaKrishnan, Synthesis, Structural Elucidation, Antioxidant, CT-DNA Binding and Molecular Docking Studies of Novel Chloroquinoline Derivatives: Promising Antioxidant and Anti-Diabetic Agents, *J. Photochem. Photobiol. B Biol.*, 2017, 173, 216–230, DOI: [10.1016/j.jphotobiol.2017.05.043](https://doi.org/10.1016/j.jphotobiol.2017.05.043).
- 18 S. Murugavel, S. Deepa, C. Ravikumar, R. Ranganathan and P. Alagusundaram, Synthesis, Structural, Spectral and Antibacterial Activity of 3,3a,4,5-Tetrahydro-2H-Benzo[g]Indazole Fused Carbothioamide Derivatives as Antibacterial Agents, *J. Mol. Struct.*, 2020, 1222, 128961, DOI: [10.1016/j.molstruc.2020.128961](https://doi.org/10.1016/j.molstruc.2020.128961).
- 19 W. Liu, E. Li, L. Liu, F. Tian, X. Luo, Y. Cai, J. Wang and X. Jin, Antifungal Activity of Compounds from *Gordonia* Sp. WA8-44 Isolated from the Gut of *Periplaneta Americana* and Molecular Docking Studies, *Heliyon*, 2023, 9(7), e17777, DOI: [10.1016/j.heliyon.2023.e17777](https://doi.org/10.1016/j.heliyon.2023.e17777).
- 20 M. I. Sulistyowaty, G. S. Putra, T. Budiati, A. W. Indrianingsih, F. Anwari, D. Kesuma, K. Matsunami and T. Yamauchi, Synthesis, In Silico Study, Antibacterial and Antifungal Activities of N-Phenylbenzamides, *Int. J. Mol. Sci.*, 2023, 24(3), 2745, DOI: [10.3390/ijms24032745](https://doi.org/10.3390/ijms24032745).
- 21 F. Wang, W. Yang and B. Zhou, Studies on the Antibacterial Activities and Molecular Mechanism of GyrB Inhibitors by 3D-QSAR, Molecular Docking and Molecular Dynamics Simulation, *Arab. J. Chem.*, 2022, 15(6), 103872, DOI: [10.1016/j.arabjc.2022.103872](https://doi.org/10.1016/j.arabjc.2022.103872).
- 22 K. M. Prabhu Kumar, B. C. Vasantha Kumar, P. R. Kumar, R. J. Butcher, H. K. Vivek, P. A. Suchetan, H. D. Revanasiddappa and S. Foro, Synthesis, Characterization, CT-DNA Binding and Docking Studies of Novel Selenated Ligands and Their Palladium Complexes, *Appl. Organomet. Chem.*, 2020, 34(6), 1–17, DOI: [10.1002/aoc.5634](https://doi.org/10.1002/aoc.5634).
- 23 K. K. Chaudhary and N. Mishra, Investigation of the Interaction Between Chalcones with CT-DNA by Molecular Docking, ADMET and Fluorescence Spectroscopy, *Proc. Natl. Acad. Sci., India, Sect. A*, 2017, 87(2), 195–206, DOI: [10.1007/s40010-017-0346-9](https://doi.org/10.1007/s40010-017-0346-9).
- 24 A. Diamanti, Z. Ganase, E. Grant, A. Armstrong, P. M. Piccione, A. M. Rea, J. Richardson, A. Galindo and C. S. Adjiman, Mechanism, Kinetics and Selectivity of a Williamson Ether Synthesis: Elucidation under Different Reaction Conditions, *React. Chem. Eng.*, 2021, 6(7), 1195–1211, DOI: [10.1039/d0re00437e](https://doi.org/10.1039/d0re00437e).
- 25 M. Rueping and B. J. Nachtsheim, A Review of New Developments in the Friedel-Crafts Alkylation - From Green Chemistry to Asymmetric Catalysis, *Beilstein J. Org. Chem.*, 2010, 6, 1–24, DOI: [10.3762/bjoc.6.6](https://doi.org/10.3762/bjoc.6.6).
- 26 Y. Otake, J. D. Williams, J. A. Rincón, O. De Frutos, C. Mateos and C. O. Kappe, Photochemical Benzylic Bromination in Continuous Flow Using BrCCl₃ and Its Application to Telescoped P-Methoxybenzyl Protection, *Org. Biomol. Chem.*, 2019, 17(6), 1384–1388, DOI: [10.1039/c9ob00044e](https://doi.org/10.1039/c9ob00044e).
- 27 Y. Jiang, W. Zhu, J. Huang, F. Luo, X. Chen, C. Fang, X. Chen, S. Liu, Y. Hu and S. A. Zhang, Simple Method for N-Arylation of Secondary Amides/Amines through a NaH-Initiated Aryne Generation Strategy, *Org. Chem. Front.*, 2023, 11(1), 12–20, DOI: [10.1039/d3qo01109g](https://doi.org/10.1039/d3qo01109g).
- 28 J. Scoccia, M. J. Castro, M. B. Faraoni, C. Bouzat, V. S. Martín and D. C. Gerbino, Iron(II) Promoted Direct Synthesis of Dibenzob[e,c]oxepin-11(6H)-One Derivatives with Biological Activity. A Short Synthesis of Doxepin, *Tetrahedron*, 2017, 73(20), 2913–2922, DOI: [10.1016/j.tet.2017.03.085](https://doi.org/10.1016/j.tet.2017.03.085).
- 29 C. C. Silveira, S. R. Mendes, L. Wolf and G. M. Martins, The Use of Anhydrous CeCl₃ as a Catalyst for the Synthesis of 3-Sulphenyl Indoles, *Tetrahedron Lett.*, 2010, 51(15), 2014–2016, DOI: [10.1016/j.tetlet.2010.02.038](https://doi.org/10.1016/j.tetlet.2010.02.038).
- 30 T. Warashina, D. Matsuura and Y. Kimura, Efficient Preparation of Dichloromethyl Alkyl Ethers and Their Application in the Formylation of Aromatic Compounds: Scope and Limitations, *Tetrahedron*, 2019, 75(5), 608–616, DOI: [10.1016/j.tet.2018.12.030](https://doi.org/10.1016/j.tet.2018.12.030).
- 31 J. Ohata, Friedel-Crafts Reactions for Biomolecular Chemistry, *Org. Biomol. Chem.*, 2024, 22(18), 3544–3558, DOI: [10.1039/d4ob00406j](https://doi.org/10.1039/d4ob00406j).
- 32 D. Cantillo, O. De Frutos, J. A. Rincon, C. Mateos and C. A. Oliver Kappe, Scalable Procedure for Light-Induced Benzylic Brominations in Continuous Flow, *J. Org. Chem.*, 2014, 79(1), 223–229, DOI: [10.1021/jo402409k](https://doi.org/10.1021/jo402409k).
- 33 S. B. Radder, R. Melavanki, S. M. Hiremath, R. Kusanur, S. S. Khemalpure and S. C. Jeyaseelan, Synthesis, Spectroscopic (FT-IR, FT-Raman, NMR & UV-Vis), Reactive (ELF, LOL, Fukui), Drug Likeness and Molecular Docking Insights on Novel 4-[3-(3-Methoxy-Phenyl)-3-Oxo-Propenyl]-Benzonitrile by Experimental and Computational Methods, *Heliyon*, 2021, 7(11), e08429, DOI: [10.1016/j.heliyon.2021.e08429](https://doi.org/10.1016/j.heliyon.2021.e08429).
- 34 R. S. Saji, J. C. Prasana, S. Muthu and J. George, Experimental and Theoretical Spectroscopic (FT-IR, FT-Raman, UV-VIS) Analysis, Natural Bonding Orbitals and Molecular Docking Studies on 2-Bromo-6-Methoxynaphthalene: A Potential Anti-Cancer Drug, *Heliyon*, 2021, 7(6), e07213, DOI: [10.1016/j.heliyon.2021.e07213](https://doi.org/10.1016/j.heliyon.2021.e07213).
- 35 M. Sima Abdollahi, E. Nemati-Kande and A. Poursattar Marjani, Experimental and DFT Studies on the FT-IR, NMR and UV/Vis Spectra of a Xanthene Derivative: The Case of



- 9-Benzoyl-3,4,5,6,7,9-Hexahydro-1h-Xanthene-1,8(2h)-Dione, *ChemistrySelect*, 2020, 5(13), 3971–3980, DOI: [10.1002/slct.201904165](https://doi.org/10.1002/slct.201904165).
- 36 K. Gullapelli, G. Brahmeshwari, M. Ravichander and U. Kusuma, Synthesis, Antibacterial and Molecular Docking Studies of New Benzimidazole Derivatives, *Egypt. J. Basic Appl. Sci.*, 2017, 4(4), 303–309, DOI: [10.1016/j.ejbas.2017.09.002](https://doi.org/10.1016/j.ejbas.2017.09.002).
- 37 D. Nahar, P. Mohite, A. Lonkar, V. R. Chidrawar, R. Dodiya, M. J. Uddin, S. Singh and B. G. Prajapati, An Insight into New Strategies and Targets to Combat Antifungal Resistance: A Comprehensive Review, *Eur. J. Med. Chem. Reports*, 2024, 10, 100120, DOI: [10.1016/j.ejmcr.2023.100120](https://doi.org/10.1016/j.ejmcr.2023.100120).
- 38 J. D. Dimitrijević, N. Solovjova, A. M. Bukonjić, D. L. Tomović, M. Milinkovic, A. Caković, J. Bogojeski, Z. R. Ratković, G. V. Janjić, A. A. Rakić, N. N. Arsenijevic, M. Z. Milovanovic, J. Z. Milovanovic, G. P. Radić and V. V. Jevtić, Docking Studies, Cytotoxicity Evaluation and Interactions of Binuclear Copper(II) Complexes with S-Isoalkyl Derivatives of Thiosalicylic Acid with Some Relevant Biomolecules, *Int. J. Mol. Sci.*, 2023, 24(15), 12504, DOI: [10.3390/ijms241512504](https://doi.org/10.3390/ijms241512504).
- 39 S. Sharma, A. Sharma and U. Gupta, Molecular Docking studies on the Anti-fungal activity of *Allium sativum* (Garlic) against Mucormycosis (black fungus) by BIOVIA discovery studio visualizer 21.1.0.0, *Ann. Antivir. Antiretrovir.*, 2021, 5(1), 028–032, DOI: [10.17352/aaa.000013](https://doi.org/10.17352/aaa.000013).
- 40 C. A. Lipinski, Rule of Five in 2015 and Beyond: Target and Ligand Structural Limitations, Ligand Chemistry Structure and Drug Discovery Project Decisions, *Adv. Drug Deliv. Rev.*, 2016, 101, 34–41, DOI: [10.1016/j.ADDR.2016.04.029](https://doi.org/10.1016/j.ADDR.2016.04.029).
- 41 M. J. Waring, *Lipophilicity in Drug Discovery*, 2010, 5(3), 235–248, DOI: [10.1517/17460441003605098](https://doi.org/10.1517/17460441003605098).
- 42 D. E. Clark, In Silico Prediction of Blood–Brain Barrier Permeation, *Drug Discov. Today*, 2003, 8(20), 927–933, DOI: [10.1016/S1359-6446\(03\)02827-7](https://doi.org/10.1016/S1359-6446(03)02827-7).
- 43 D. Osmaniye, N. Baltacı Bozkurt, S. Levent, G. Benli Yardımcı, B. N. Sağlık, Y. Ozkay and Z. A. Kaplancıklı, Synthesis, Antifungal Activities, Molecular Docking and Molecular Dynamic Studies of Novel Quinoxaline-Triazole Compounds, *ACS Omega*, 2023, 8(27), 24573–24585, DOI: [10.1021/acsomega.3c02797](https://doi.org/10.1021/acsomega.3c02797).
- 44 D. Zaeifi, A. Najafi and R. Mirnejad, Molecular Dynamics Simulation of Antimicrobial Peptide CM15 in Staphylococcus Aureus and Escherichia Coli Model Bilayer Lipid, *Iran. J. Biotechnol.*, 2023, 21(2), 15–26, DOI: [10.30498/ijb.2023.337246.3344](https://doi.org/10.30498/ijb.2023.337246.3344).
- 45 Clinical and Laboratory Standards Institute, *Performance Standards for Antimicrobial Disk Susceptibility Tests: Approved Standard - Eleventh Edition*, 2012, vol. 32, M02-A11.
- 46 X. Wang, H. Y. Fu, W. He, Y. T. Xiang, Z. C. Yang, Y. Kuang and S. X. Yang, Synthesis and Antibacterial Activity Evaluation of Biphenyl and Dibenzofuran Derivatives as Potential Antimicrobial Agents against Antibiotic-Resistant Bacteria., *Curr. Issues Mol. Biol.*, 2022, 44(9), 4087–4099, DOI: [10.3390/cimb44090280](https://doi.org/10.3390/cimb44090280).
- 47 V. L. Barnes, D. M. Heithoff, S. P. Mahan, J. K. House and M. J. Mahan, Antimicrobial Susceptibility Testing to Evaluate Minimum Inhibitory Concentration Values of Clinically Relevant Antibiotics, *STAR Protoc.*, 2023, 4(3), 102512, DOI: [10.1016/j.xpro.2023.102512](https://doi.org/10.1016/j.xpro.2023.102512).
- 48 B. GKowalska-Krochmal and R. Dudek-Wicher, The Minimum Inhibitory Concentration of Antibiotics: Methods, Interpretation, Clinical Relevance, *Pathogens*, 2021, 10(2), 1–21, DOI: [10.3390/pathogens10020165](https://doi.org/10.3390/pathogens10020165).
- 49 M. Sunita, B. Anupama, B. Ushaiyah and C. Gyana Kumari, Synthesis, Characterization, DNA Binding and Cleavage Studies of Mixed-Ligand Copper (II) Complexes, *Arab. J. Chem.*, 2017, 10, S3367–S3374, DOI: [10.1016/j.arabjc.2014.01.017](https://doi.org/10.1016/j.arabjc.2014.01.017).
- 50 K. Yi, X. Wang, S. K. Filippov and H. Zhang, Emerging CtDNA Detection Strategies in Clinical Cancer Theranostics, *Smart Med.*, 2023, 2(4), 1–17, DOI: [10.1002/smmd.20230031](https://doi.org/10.1002/smmd.20230031).
- 51 C. Levine, H. Hiasa and K. J. Marians, DNA Gyrase and Topoisomerase IV: Biochemical Activities, Physiological Roles during Chromosome Replication, and Drug Sensitivities, *Biochim. Biophys. Acta*, 1998, 1400(1–3), 29–43, DOI: [10.1016/S0167-4781\(98\)00126-2](https://doi.org/10.1016/S0167-4781(98)00126-2).

